Local caspase activation interacts with Slit-Robo signaling to restrict axonal arborization

Douglas S. Campbell and Hitoshi Okamoto

Laboratory for Developmental Gene Regulation, RIKEN Brain Science Institute, Wako, Saitama 351-0198, Japan

In addition to being critical for apoptosis, components of the apoptotic pathway, such as caspases, are involved in other physiological processes in many types of cells, including neurons. However, very little is known about their role in dynamic, nonphysically destructive processes, such as axonal arborization and synaptogenesis. We show that caspases were locally active in vivo at the branch points of young, dynamic retinal ganglion cell axonal arbors but not in the cell body or in stable mature arbors. Caspase activation, dependent on Caspase-3, Caspase-9, and p38 mitogen-activated protein kinase (MAPK), rapidly increased at branch points corresponding with branch tip addition. Time-lapse imaging revealed that knockdown of Caspase-3 and Caspase-9 led to more stable arbors and presynaptic sites. Genetic analysis showed that Caspase-3, Caspase-9, and p38 MAPK interacted with Slit1a-Robo2 signaling, suggesting that localized activation of caspases lie downstream of a ligand receptor system, acting as key promoters of axonal branch tip and synaptic dynamics to restrict arbor growth in vivo in the central nervous system.

Introduction

The formation of functional synaptic connections is critical for the normal operation of the nervous system. In the central nervous system (CNS), synapse formation depends on the regulated elaboration of the arbors (consisting of branches) of pre- and postsynaptic cell axons and dendrites, processes that can occur concurrently (Waites et al., 2005; Meyer and Smith, 2006; Ruthazer et al., 2006; Jin and Garner, 2008; Gibson and Ma, 2011). The processes of arborization and synaptogenesis are crucial in defining neuronal morphology and synaptic connectivity (Lin and Koleske, 2010). Abnormalities in arbor structure can lead to changes in behavior (Smear et al., 2007) and neurodevelopmental disorders (Wong, 2008). Arbor and synaptic structure are often affected early in the progression of neurodegenerative conditions (Wishart et al., 2006; Saxena and Caroni, 2007), illustrating the fundamental importance of the regulation of these processes in the nervous system.

The vertebrate retinotectal projection has become a powerful model system for the study of axon pathfinding, arborization, and synaptogenesis (Dingwell et al., 2000; Hutson et al., 2004;

Cohen-Cory, 2007; Poulain et al., 2010). The growth cones at the tips of retinal ganglion cell (RGC) axons navigate along a stereotypical pathway from the retina to their target, the optic tectum in the midbrain. Upon reaching the tectum growth cones change their morphology with the production of branches to develop an arbor, accompanied by the formation of synapses, both of which are highly dynamic processes (Harris et al., 1987; Meyer and Smith, 2006; Ruthazer et al., 2006; Campbell et al., 2007). A variety of ligand receptor systems have been identified taking part in these processes, including brain-derived neurotrophic factor (Cohen-Cory and Fraser, 1995; Alsina et al., 2001), Netrin-1 (Manitt et al., 2009), Sema3A (Semaphorin 3A; Campbell et al., 2001), and Slit1a-Robo2 (Roundabout 2) signaling (Campbell et al., 2007). However, unlike the intensive investigation of the intracellular signaling pathways acting downstream of ligand receptor systems operating in growth cone guidance (O'Donnell et al., 2009; Bashaw and Klein, 2010), our understanding of the intracellular signaling pathways regulating arborization and synaptogenesis remains much more limited.

Neurons are compartmentalized into a cell body, an axon, and dendrites. Somaless *Xenopus laevis* axonal growth cones

The Rockefeller University Press $30.00
J. Cell Biol. Vol. 203 No. 4 657–672
www.jcb.org/cgi/doi/10.1083/jcb.201303072

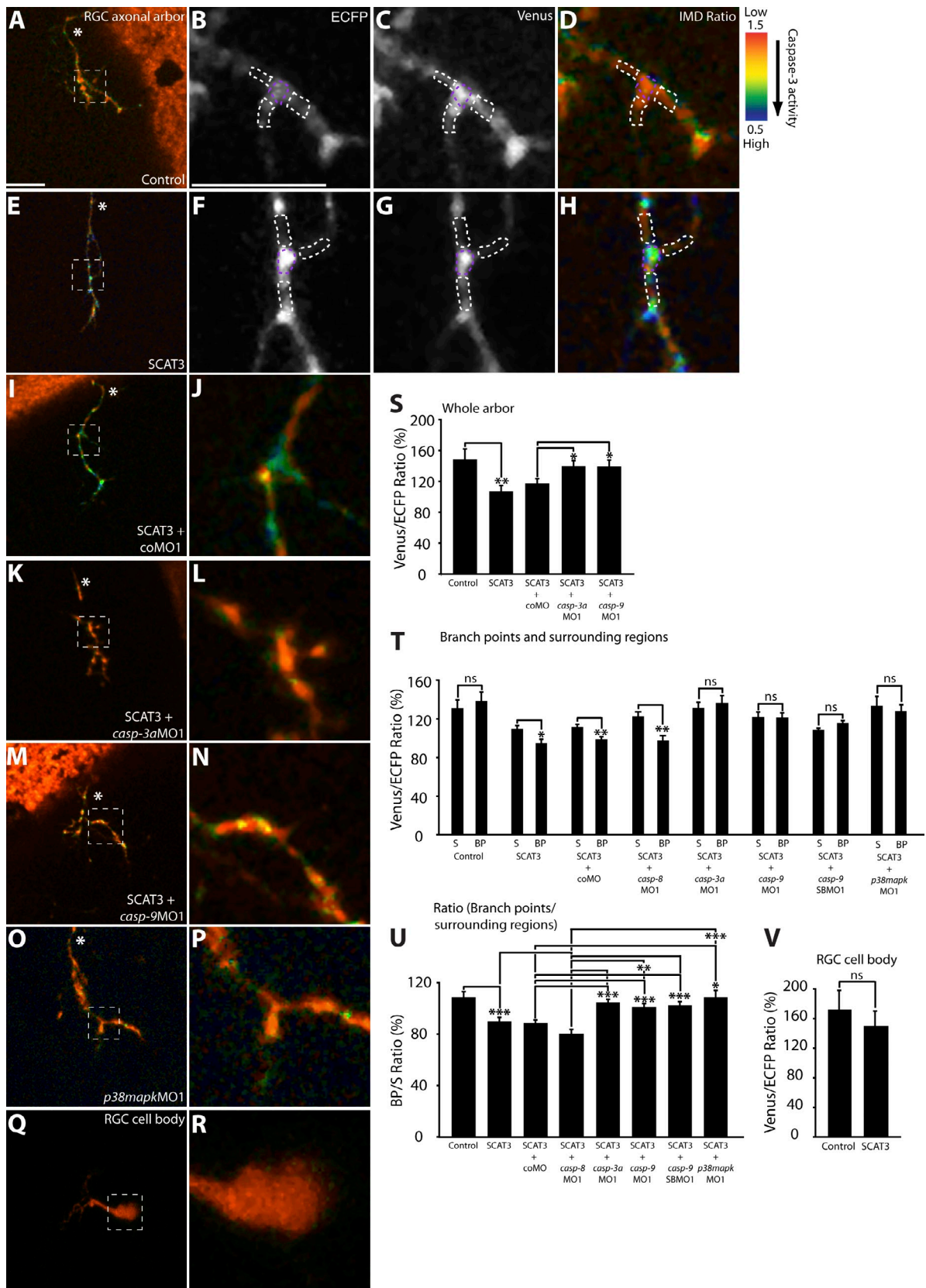JCB **657**

THE JOURNAL OF CELL BIOLOGY

Figure 1.   **Local caspase activation at branch points in young RGC arbors.** (A, D, E, and H–R) Representative IMD ratio images of 80-hpf live RGC arbors in the optic tectum (A, D, E, and H–P) and an RGC cell body (Q and R) in the retina. Caspase activation is represented by the pseudocolors that correspond to the Venus/ECFP ratio (1.5–0.5). Red represents low caspase activation, and violet represents high caspase activation. (A, D, E, and H–P) Control (A and D), SCAT3 (E and H), SCAT3 + coMO (I and J), SCAT3 + c*asp-3a*MO1 (K and L), SCAT3 + *casp-9*MO1 (M and N), and SCAT3 + *p38mapk*MO1 (O and P) are shown. (B–D and G) ECFP channel (B and D) and Venus channel (C and G) of SCAT3- and control-expressing arbors are also shown.

are able to undergo chemotropic responses in vitro (Campbell and Holt, 2001; Ming et al., 2002) and to navigate to and arborize in the optic tectum in vivo (Harris et al., 1987), suggesting a role for local signaling pathways. Indeed, the structural compartmentalization of neurons allows the partitioning of cellular signaling pathways, such as those regulating protein synthesis and degradation to axons and/or dendrites (Steward and Schuman, 2003; Cajigas et al., 2010; Bingol and Sheng, 2011; Jung et al., 2011). This could allow very precise local control of neuronal morphology and remodeling critical for the correct development and function of neurons. Caspases are an example of a protease system, originally identified for their critical roles in apoptosis and cytokine processing (Creagh and Martin, 2001; Ulukaya et al., 2011). More recently, localized nonapoptotic roles for caspases have been identified (Kuranaga and Miura, 2007; D'Amelio et al., 2012; Hyman and Yuan, 2012). For example, in neurons, caspases may be active and act in axons or dendrites, mediating the chemotropic responses of *Xenopus* retinal growth cones (Campbell and Holt, 2003), dendritic pruning during metamorphosis in *Drosophila melanogaster* (Kuo et al., 2006; Williams et al., 2006), mammalian long-term depression (Li et al., 2010; Jiao and Li, 2011), and songbird learning (Huesmann and Clayton, 2006). However, the role of the apoptotic pathway and the principles underlying its regulation in local nonapoptotic roles in neurons in vivo, such as during the processes of axonal arborization and synaptogenesis, remain largely unknown.

To address these issues, we imaged caspase activity in the CNS in vivo, in the intact living zebrafish embryo. We show that caspase activity is very local, at the branch points of young dynamic RGC axonal arbors, in a Caspase-3–, Caspase-9–, and p38 MAPK–dependent manner, but not in RGC cell bodies. Time-lapse imaging revealed that caspase activity undergoes rapid activation at branch points during branch tip formation. In contrast, older, more stable arbors have reduced levels of caspase activation. Furthermore, a reduction of Caspase-3, Caspase-9, and p38 MAPK function leads to more stable arbors and interactions with Slit1a-Robo2 signaling to restrict arbor growth and synaptogenesis. Our findings suggest that local caspase activation is a key promoter of axon remodeling in vivo in the vertebrate CNS.

Results

Local caspase activation at branch points of young RGC arbors

To investigate whether caspases play nonapoptotic roles in the processes of arborization and synaptogenesis, we performed mRNA in situ hybridization at 80 h postfertilization (hpf) with zebrafish *casp-3a* (*caspase-3a*) and *casp-9* (*caspase-9*), key effector and initiator caspases of the intrinsic apoptotic pathway, and *casp-8* (*caspase-8*), an activator of Caspase-3 in the extrinsic apoptotic pathway, respectively (Ulukaya et al., 2011). *casp-3a* and *casp-9* are strongly expressed in the RGC layer of the retina and throughout the tectum (Fig. S1, A–D), whereas *casp-8* showed a similar though much weaker expression pattern (Fig. S1, E and F). Next, we used the caspase activity reporter, SCAT3 (sensor for activated caspases based on fluorescence resonance energy transfer [FRET] 3; Takemoto et al., 2003, 2007) to reveal the temporal and spatial pattern of caspase enzymatic activity in the retinotectal system in vivo. SCAT3 consists of ECFP and Venus separated by a peptide linker region containing a DEVD (Asp-Glu-Val-Asp) consensus Caspase-3 cleavage site. The DEVD cleavage site specificity is conserved for zebrafish Caspase-3 (Yabu et al., 2001). Because the peptide linker region of SCAT3 is cleaved by caspase activity, its activity is reported as a decrease in the Venus/ECFP ratio, representing a decrease in FRET (Takemoto et al., 2003). SCAT3 or control constructs lacking the cleavage site were transiently expressed in RGCs and tectal cells (Materials and methods; Campbell et al., 2007; Sato et al., 2007). SCAT3-expressing 80-hpf RGC axonal arbors showed a significant decrease in the Venus/ECFP over the whole arbor and at branch points compared with surrounding regions (regions of interest) defined in the legend to Fig. 1, relative to arbors expressing the control construct (Fig. 1, A–H and quantified in S–U).

To demonstrate that the decrease in Venus/ECFP ratio observed for SCAT3-expressing arbors primarily reflected Caspase-3 activity, we used antisense morpholino (MO) oligonucleotides to partially knockdown Caspase-3 function. A previously published MO against zebrafish *casp-3a* (*casp-3a*MO1; Yamashita et al., 2008) blocked the decrease in the SCAT3 Venus/ECFP ratio over the whole arbor and at branch points compared with surrounding regions, whereas a five–base pair mismatch control MO (controlMO [coMO]) did not (Fig. 1, I–L and quantified in S–U). Additionally, knockdown of *casp-8* (*casp-8*MO1; Sidi et al., 2008), whose activity may partially cleave SCAT3 in vitro (Takemoto et al., 2003), did not (Fig. 1, T and U). Because it has not previously been reported that SCAT3 is an effective reporter of Caspase-3 activity in the zebrafish, we performed additional control experiments (Fig. S2).

To further confirm apoptotic pathway activation of SCAT3, we knocked down *casp-9*, a key initiator caspase, which proteolytically cleaves and activates executioner caspases, such as Caspase-3 (Ulukaya et al., 2011), and whose activity may partially cleave SCAT3 in vitro (Takemoto et al., 2003). Compared with coMO morphant arbors, knockdown of Caspase-9 function with two

---

The region enclosed by the dashed squares in A, E, I, K, M, O, and Q are magnified in B–D, F–H, J, L, N, P, and R. (S) Quantification of Venus/ECFP ratios across the whole arbor. Branch points were determined as covering a distance of 1 µm or less away from where a branch tip joins an arbor. Surrounding regions were determined at a distance of 1 µm away from a branch tip and 2 µm in length, covering the width of the branches. (B–D and F–H) Examples illustrating regions of interest for the quantification of the Venus/ECFP ratio at branch points (purple dashed areas) and surrounding regions (white dashed areas) for control- and SCAT3-expressing arbors, respectively. (T) Quantification of Venus/ECFP ratios at branch points (BP) and surrounding regions (S). (U and V) Presented as a ratio of branch points/surrounding regions (U) and RGC cell bodies (V). White asterisks indicate the parent axon. 19–28 RGC arbors were analyzed in S. 29–36 branch points and 87–108 surrounding regions were analyzed in T and U. 15–16 RGC cell bodies were analyzed in V. Error bars represent SEMs. *, P < 0.05; **, P < 0.01; ***, P < 0.001. Bars, 10 µm. The image in E of a SCAT3-expressing arbor is shown again in Figs. 5 A and S2 C. The magnified image in H also is shown again in Fig. 5 B.
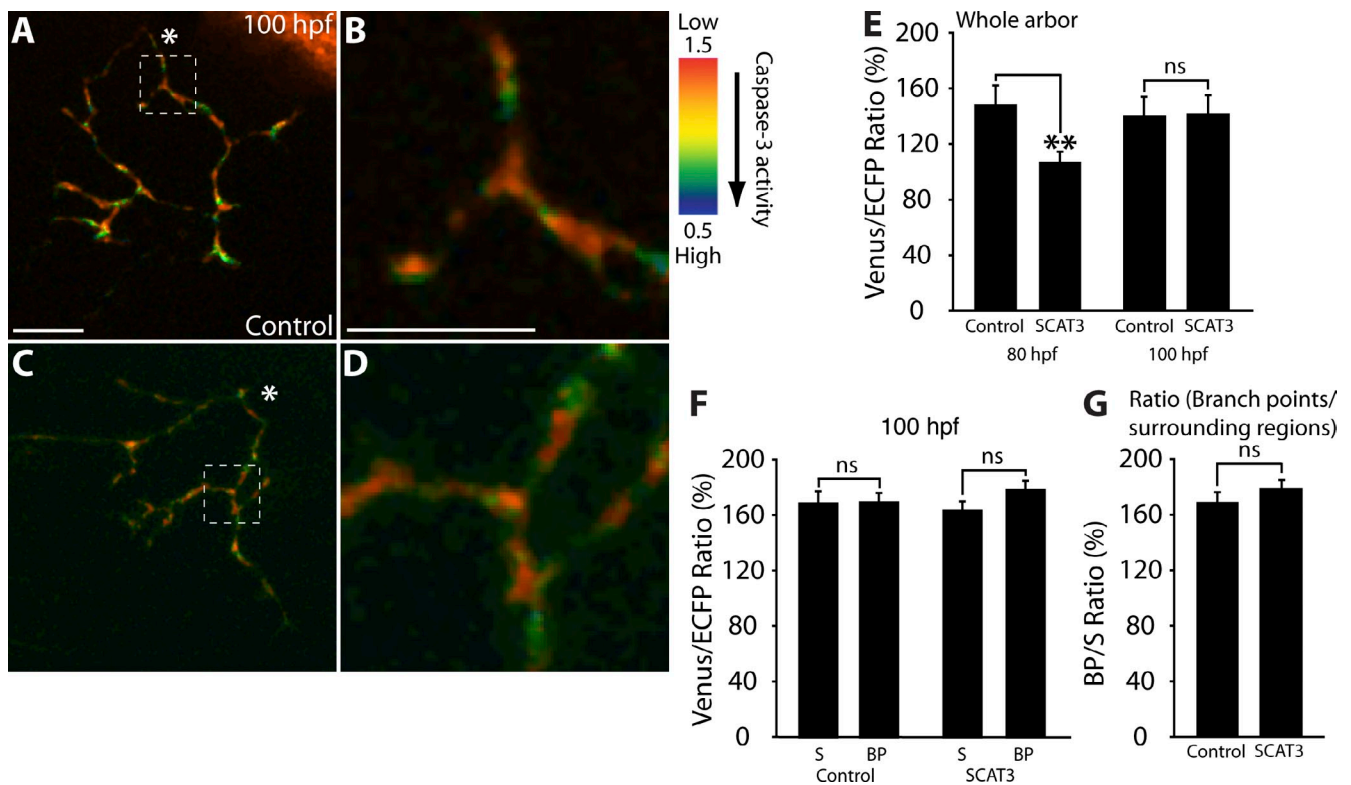
Figure 2. **Caspase activity is undetectable in older RGC arbors.** (A–D) Representative IMD ratio images of 100-hpf live RGC arbors in the optic tectum; caspase activation is represented by the pseudocolors that correspond to the Venus/ECFP ratio (1.5–0.5). Red represents low caspase activation and violet represents high caspase activation. (A–D) Control (A and B) and SCAT3 (C and D) images are presented. The region enclosed by the dashed squares in A and C are magnified in B and D. (E–G) Quantification of Venus/ECFP ratios across the whole arbor for both 80-hpf (E; data as in Fig. 1 S) and 100-hpf (F) arbors at branch points (BP) and surrounding regions (S) presented as a ratio of branch points/surrounding regions (G). White asterisks indicate the parent axon. Dorsal views are shown, and anterior is up. 10–12 RGC arbors were analyzed per condition. Error bars represent SEMs. **, P < 0.01. Bars, 10 µm.

different MOs (translation-blocking *casp-9*MO1 and splice-blocking [SB] *casp-9*SBMO1; Sidi et al., 2008) blocked the decrease in Venus/ECFP ratio (Fig. 1, M and N and quantified in S–U), indicating that SCAT3 reports caspase activation. Caspase activation was also blocked by knockdown of p38 MAPK, expressed in zebrafish RGCs (Krens et al., 2006), and which we have shown previously to be upstream of Caspase-3 activation in retinal growth cones (Fig. 1, O and P and quantified in T and U; Campbell and Holt, 2003; Hsu et al., 2011 [*p38mapk*MO1]). As there is a low amount of apoptotic cell death in zebrafish RGCs at 80 hpf (Biehlmaier et al., 2001), we next tested that the lack of apoptosis observed is caused by lack of caspase activation in RGC cell bodies. SCAT3- or control-expressing 80-hpf RGC cell bodies did not show caspase activation (Fig. 1, Q and R and quantified in V). We were also unable to detect significant caspase activation in the dendrites of 80-hpf and 100-hpf tectal cells (Fig. S3).

Caspase activity rapidly increases upon branch tip formation

Caspase activation at branch points in 80-hpf RGC arbors correlates with a period during which they are highly dynamic (Stuermer, 1988; Meyer and Smith, 2006; Campbell et al., 2007). Older (100 hpf) arbors that we have previously shown to be more stable (Stuermer, 1988; Campbell et al., 2007) had a

high Venus/ECFP ratio, i.e., low caspase activation (Fig. 2, A–D and quantified in E–H). To establish whether caspase activation is dynamically regulated, we visualized branch point additions and retractions directly over time in the same arbors, via time-lapse imaging of 80-hpf and 100-hpf arbors expressing SCAT3 every 5 min for ∼2 h. For 80-hpf arbors, we observed branch tip additions and measured the Venus/ECFP ratio for the region of the arbor that would become a branch point in the next 5 min and a neighboring region of the same arbor that would not, i.e., dynamic versus nondynamic areas of the same arbor (Fig. 3 A, region of interest defined in the legend and imaging scheme). We found that a region of an arbor that became a branch point in 5 min underwent a significant increase in caspase activation during the 5-min interval between time points compared with a neighboring region of an arbor that did not become a branch point (Fig. 3, B–E and quantified in F and G; and Video 1). Imaging of stable branch points and neighboring regions of 100-hpf arbors, which do not have a branch point, nor will they develop one during the 5-min imaging interval (Fig. 3 H), did not show significant caspase activation (Fig. 3, I–L and quantified in M and N; and Video 2). Thus, caspase activity rapidly increases (within 5 min) at branch points, immediately before or during branch tip formation, whereas a reduction of caspase activation directly correlates with increased branch tip stability. We were unable to detect significant caspase activation at branch points
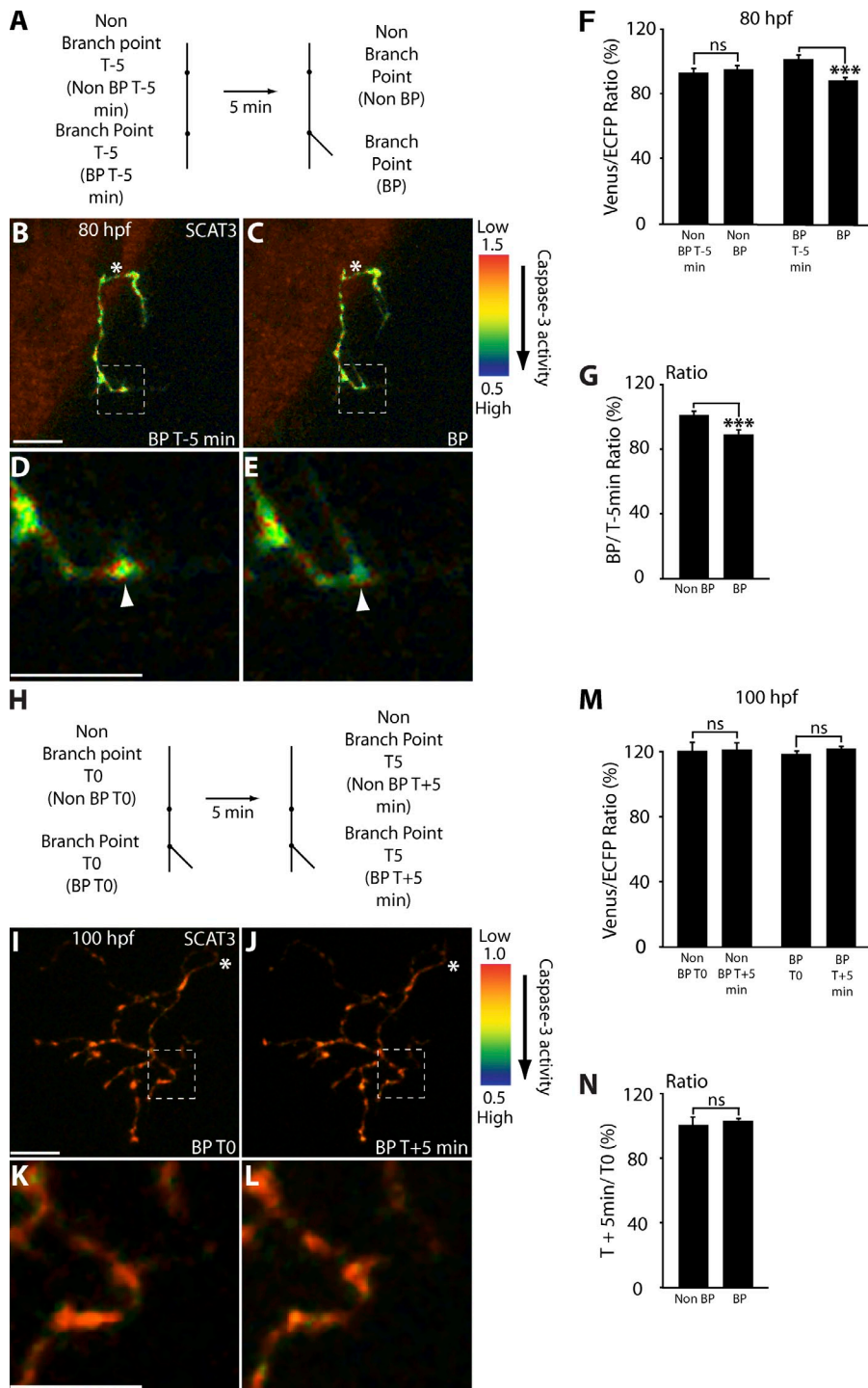
Figure 3. **Caspase activity rapidly increases upon young RGC arbor branch tip formation.** (A) Imaging analysis scheme for 80-hpf arbors expressing SCAT3-forming branches during the 5-min imaging interval. Branch points were determined as covering a distance of 2 µm or less away from where a branch tip joins, and arbor nonbranch points were 5–20 µm away from a branch tip and 3 µm in length, covering the width of the branches as for surrounding regions (Fig. 1). (B–E) Representative IMD images of an 80-hpf RGC arbor expressing SCAT3. Caspase activation is represented by the pseudocolors that correspond to the Venus/ECFP ratio 1.5–0.5 or 1.0–0.5. Red represents low caspase activation, and violet represents high caspase activation. (B–D) 5 min before branch point formation (BP T − 5 min; B) and after branch tip (BP) formation (C). The region enclosed by the dashed squares in B and C are magnified in D and E. (F and G) Quantification of the Venus/ECFP ratio (F) comparing changes in arbors between regions that do or do not lead to the formation of branch points as in the scheme in A and presented as ratios (G). (H) Imaging analysis scheme for 100-hpf arbors expressing SCAT3 that are stable during the 5-min imaging interval. (I–L) Representative IMD images of a 100-hpf RGC arbor expressing SCAT3 that possesses branch points (BP T0; I), which remain stable during the 5-min imaging interval (BP T + 5 min; J). The regions enclosed by the dashed squares in I and J are magnified in K and L. (M and N) Quantification of the Venus/ECFP ratio (M) comparing changes in arbors between stable branch tips and regions that do not form branch tips as in the scheme in H and presented as ratios (N). White arrowheads depict the region in D that will become a branch point in E. White asterisks indicate the parent axon. 37 branch point additions and nonbranch points in six arbors were analyzed for 80-hpf arbors. 30 stable branch points from seven arbors were analyzed for 100-hpf arbors. Dorsal views are shown, and anterior is up. Error bars represent SEMs. ***, $P < 0.001$. Bars, 10 µm.

where branch tips had undergone recent retractions (i.e., within 5 min; Fig. S4). However, we were able to detect a significant decrease in caspase activation between regions of an arbor that underwent recent branch point retractions compared with those that had undergone recent branch tip additions (Fig. S4 H).

Caspase-3, Caspase-9, and p38 MAPK promote RGC axonal arbor and presynaptic dynamics in vivo

Our in vivo imaging studies using SCAT3 indicate that caspase activation is more active before and/or during branch tip formation,

suggesting that it may promote arbor dynamics. We performed time-lapse imaging every 15 min for 5 h of 80-hpf arbors expressing the presynaptic marker YFP-Rab3 (Campbell et al., 2007), taking advantage of our observations that *casp-3a*MO1, *casp-9*MO1, and *p38mapk*MO1 were able to reduce caspase activation (Fig. 1, G–J and quantified in M–O), that there is no increase in apoptosis from the administration of the MOs, and that the RGC axons of the morphants project normally to the optic tectum (Fig. S5). *casp-3a*MO1, *casp-9*MO1, and *p38mapk*MO1 morphant arbors showed a reduction in dynamic branch tips accompanied by an increase in stable branch tips, decreased

Figure 4. **Capase-3, Caspase-9, and p38 MAPK promote RGC axon arbor dynamics.** (A, C, E, G, and I) Tracings of arbors at 80–85 hpf expressing YFP-Rab3. Images represent WT (A), coMO (C), *casp-3a*MO1 (E), *casp-9*MO1 (G), and *p38mapk*MO1 (I) morphant arbors every hour during a 5-h time-lapse imaging. All show dorsal views. Black, stable branch tips; red, eliminated tips; green, added tips; blue, tips that were added then eliminated during imaging. (B, D, F, H, and J). The proportion of branch tips in each category. These graphs are derived from analysis of a single arbor in a single experiment. (K and L) Branch tip additions (K) and retractions (L) are shown in the graphs. (N and O) Presynaptic puncta gain (N) and loss (O) are presented as a percentage of initial branch tip or presynaptic puncta, respectively. (M and P) Total branch tip (M) and presynaptic puncta lifetimes (P) include all branch tips or presynaptic puncta present at one or more time points. (Q and R) Total branch tip (Q) and presynaptic puncta lifetime distribution (R) are shown. 9–13 RGC arbors were analyzed per condition. Tracings are dorsal views; anterior is up. Error bars represent SEMs. *, $P < 0.05$; **, $P < 0.01$; ***, $P < 0.001$. Bar, 10 µm.
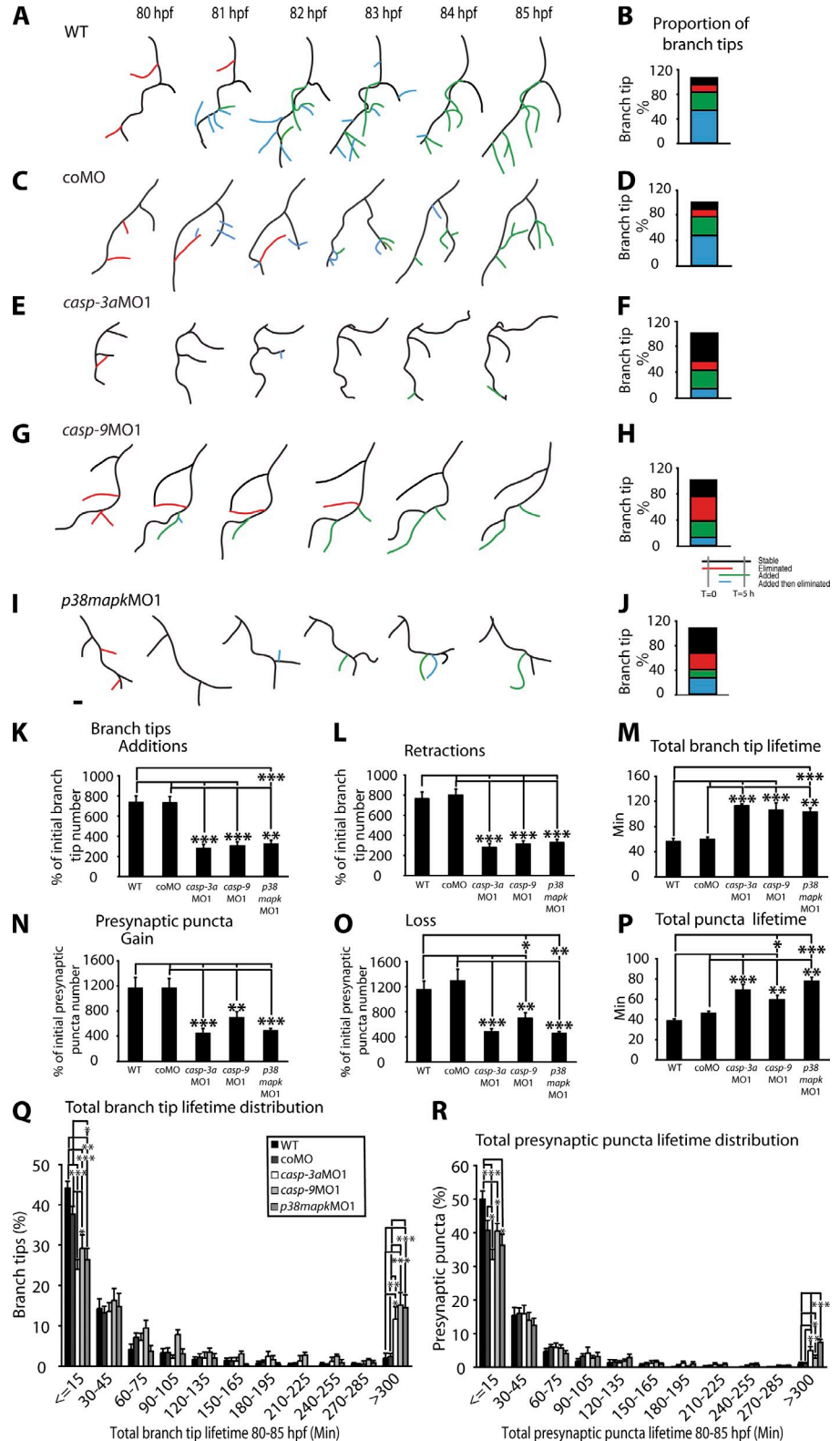
branch tip additions, and retractions to approximately one third of those of wild-type (WT) or coMO arbors (Fig. 4, A–L; and Videos 3, 4, 5, 6, and 7). This was accompanied by an approximate doubling in total branch tip lifetimes, a significant decrease in short-lived branch tips (with a lifetime of ≤15 min), and an increase in the proportion of branch tips present

throughout the whole imaging period (Fig. 4, M and Q; and Videos 3, 4, 5, 6, and 7). Similar effects were observed for presynaptic puncta gain, loss, total puncta lifetimes, the proportion of short-lived puncta, and the proportion of puncta present during the entire imaging period (Fig. 4, N–P and R; and Videos 3, 4, 5, 6, and 7). Our findings indicate that
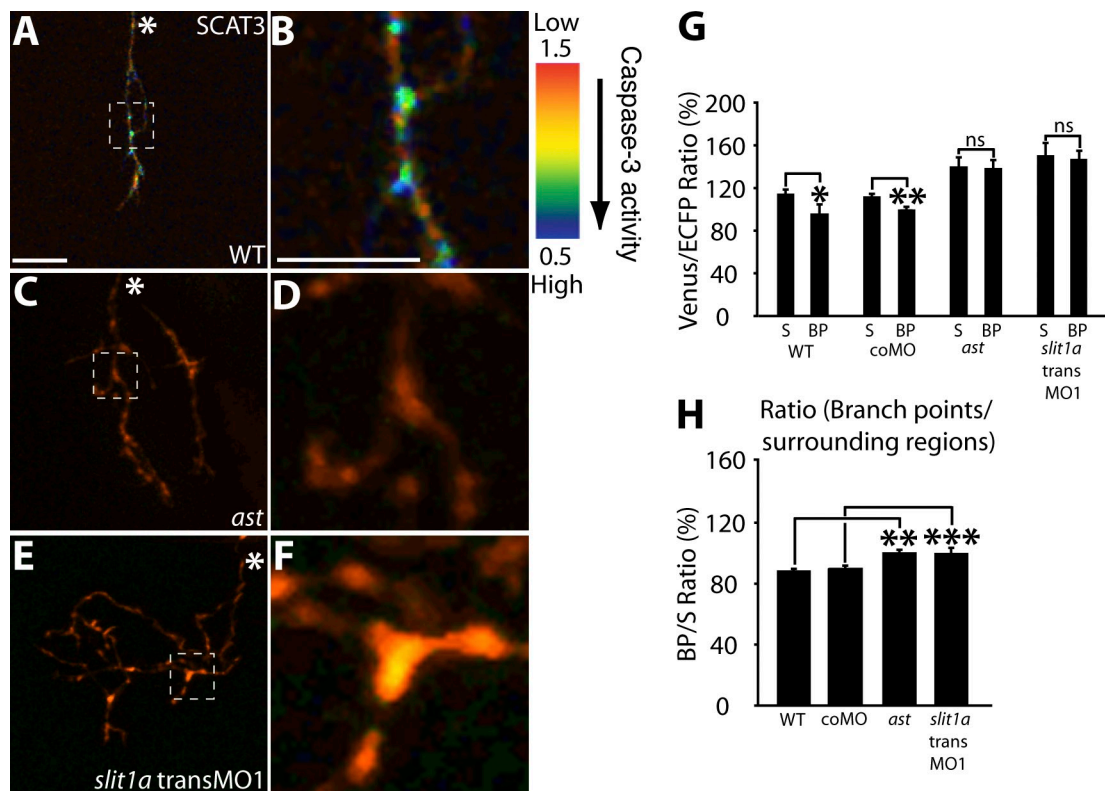
Figure 5. **Caspase activation is reduced in RGC arbors with impaired Slit1a-Robo2 signaling.** (A–F) Representative IMD ratio images of 80-hpf live RGC arbors in the optic tectum expressing SCAT3. Caspase activation is represented by the pseudocolors that correspond to the Venus/ECFP ratio (1.5–0.5). Red represents low caspase activation, and violet represents high caspase activation. WT (A and B), *ast* (C and D), and *slit1a* transMO1 (E and F) are shown. The regions enclosed by the dashed squares in A, C, and E are magnified in B, D, and F. (G and H) Quantification of Venus/ECFP ratios (G) at branch points (BP) and surrounding regions (S) presented as a ratio of branch points/surrounding regions (H). White asterisks indicate the parent axon. 15–35 branch points and 45–105 surrounding areas were analyzed per condition. Dorsal views are shown, and anterior is up. Error bars represent SEMs. *, P < 0.05; **, P < 0.01; ***, P < 0.001. Bars, 10 µm. The image in A of a SCAT3-expressing arbor is shown again in Figs. 1 E and S2 C. The magnified image in B also is shown again in Fig. 1 H.

Caspase-3, Caspase-9, and p38 MAPK are key promoters of RGC axon arbor dynamics.

Caspase-3, Caspase-9, and p38 MAPK interact with Slit1a-Robo2 signaling to restrict arbor growth

The knockdown of Caspase-3 and Caspase-9 function leads to more stable branch tips and presynaptic sites, which is very similar to loss of Slit1a-Robo2 signaling on RGC arbor dynamics (Campbell et al., 2007). This observation in combination with the observations that Robo2 acts cell autonomously in RGCs (Campbell et al., 2007) and that the apoptotic pathway is locally activated in RGC arbors leads to a possible model in which Caspase-3 and Caspase-9 might be part of the mechanism downstream of Slit1a-Robo2 signaling, promoting arbor dynamics and restricting growth. To examine this, we expressed SCAT3 and observed caspase activity in 80-hpf *astray (ast)/ robo2* mutant, *slit1a* translation-blocking (trans) MO1 (*slit1a* transMO1), and morphant arbors at a dose known to increase arbor size and complexity (Campbell et al., 2007). Compared with age-matched WT or control morphant arbors, we were unable to detect an increase in caspase activation at branch points relative to surrounding regions (Fig. 5, A–F and quantified in G and H), proposing that a reduction of Slit1a or Robo2

function leads to the earlier down-regulation of caspase activation in RGC arbors and that caspase activation may act in the Slit1a-Robo2 signaling pathway.

As a functional test of the aforementioned model, we examined gene–dosage effect interactions between *ast/robo2*, *slit1a*, *casp-3a*, and *casp-9*. We observed 80-hpf YFP-Rab3–expressing RGC arbors from WT, *ast*, *ast/+*, *robo2*, or *slit1a* morphant embryos injected with either nothing, coMO, *casp-3a*MO1, or *casp-9*MO1. Loss of one copy of Robo2 in *ast/+* or knockdown of *robo2*, *slit1a*, *casp-3a*, or *casp-9* led to arbors that were indistinguishable to WT or coMO arbors by all our quantitative parameters (*ast/+*, *robo2*SBMO, *slit1a* transMO1 [low dose], *casp-3a*MO1, and *casp-9*MO1 compared with WT and coMO; Fig. 6, A–G and quantified in M–R). However, combining the reduction of Robo2 or Slit1a function with either knockdown of *casp-3a* or *casp-9* led to significant increases in branch tip number, arbor area, total arbor length, arbor order, and presynaptic puncta number, which were similar in size and complexity to *ast* mutant arbors (*ast/+*; *casp-3a*MO1, *robo2*SBMO; *casp-9*MO1, *slit1a* transMO1 [low dose]; *casp-3aMO1*, *slit1a* transMO1 [low dose]; *casp-9*MO1, and *ast* compared with control conditions; Fig. 6, H–L and quantified in M–R; Campbell et al., 2007). Combining the knockdown of *p38mapk* with the knockdown of *slit1a* or *robo2* also led to an
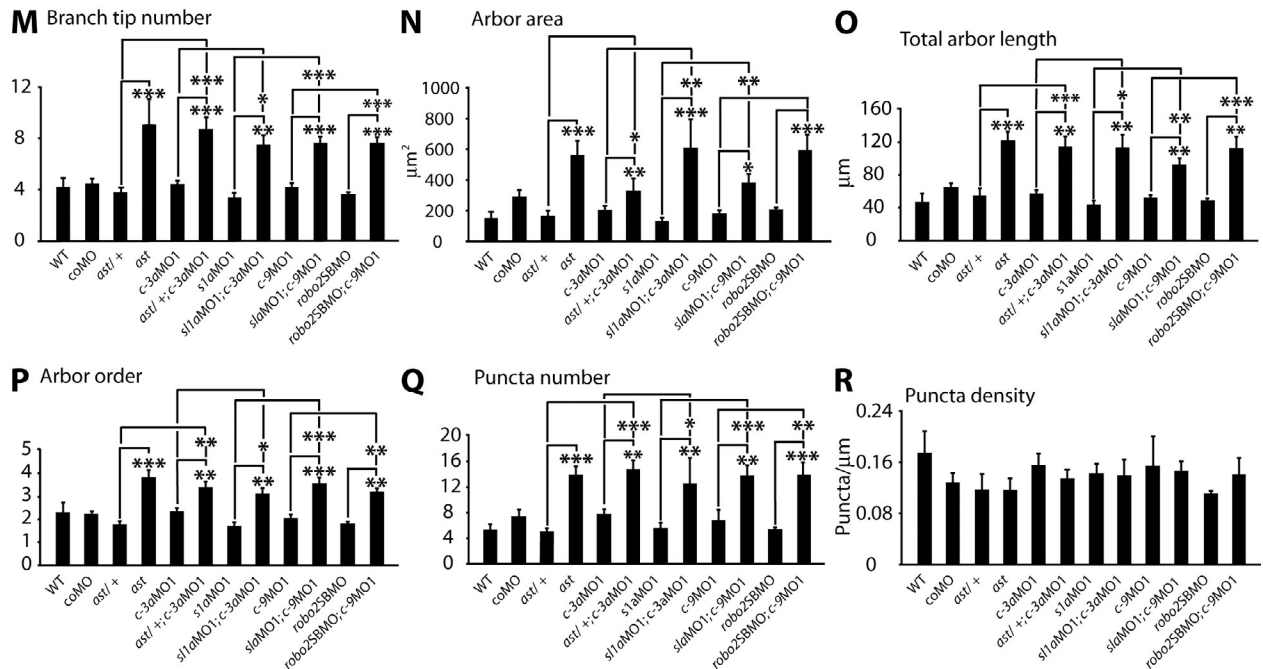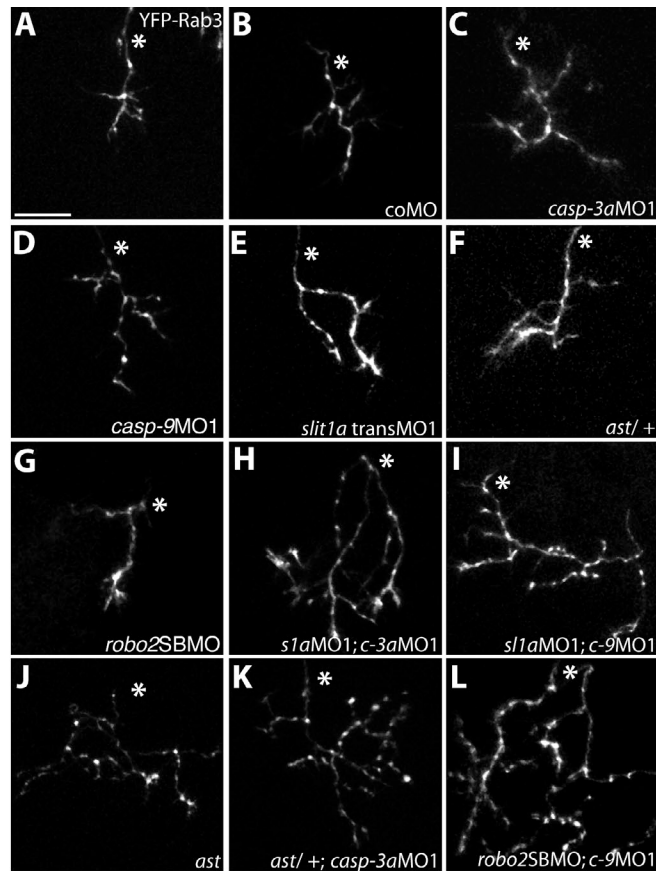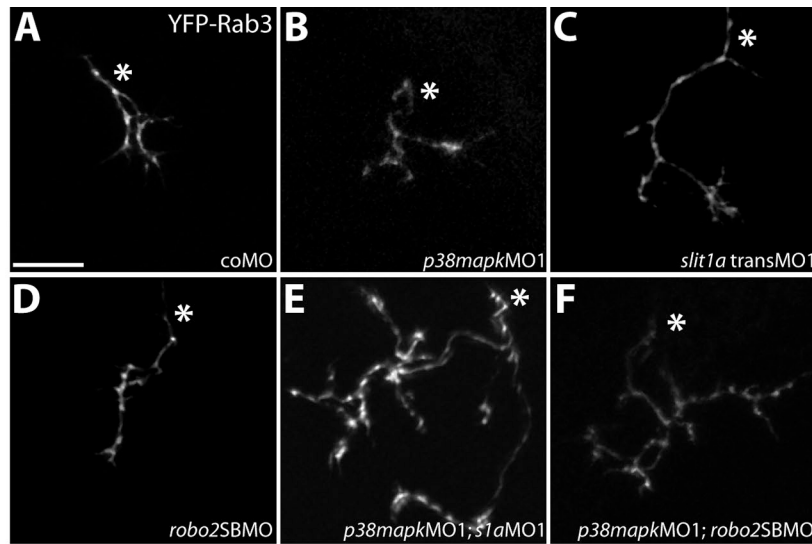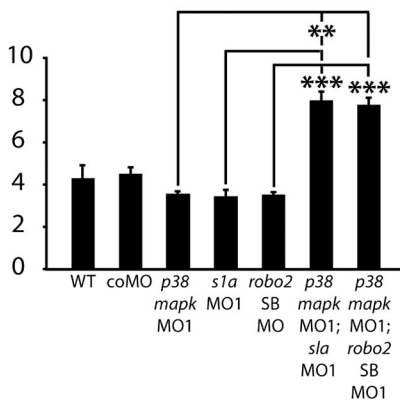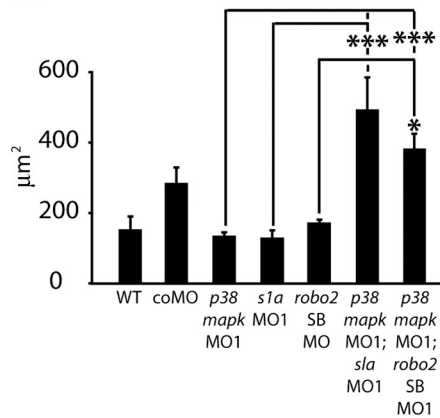
Figure 6. **Caspases-3 and -9 interact with Slit1a-Robo2 signaling to restrict arbor size.** (A–L) Maximum intensity projections of 80-hpf RGC arbors in the optic tectum expressing YFP-Rab3. WT (A), coMO (B), *casp-3a*MO1 (C), *casp-9*MO1 (D), *slit1a* transMO1 (low dose; E), *ast/+* (F), *robo2*SBMO1 (low dose; G), *slit1a* transMO1 (low dose); *casp-3a*MO1 (H), *slit1a* transMO1 (low dose; I), *ast* (J), *ast/+; casp-3a*MO1 (K), and *robo2*SBMO1 (low dose); *casp-9*MO1 (L) are shown. (M–R) Quantification of arbor parameters: branch tip number (M), arbor area (N), total arbor length (O), arbor order (P), presynaptic puncta number (Q), and puncta density (R). 7–15 arbors were analyzed per condition. Part of the *ast* data is obtained from Campbell et al. (2007). Dorsal views are shown, and anterior is up. White asterisks indicate the parent axon. Error bars represent SEMs. *, P < 0.05; **, P < 0.01; ***, P < 0.001. Bar, 10 µm.
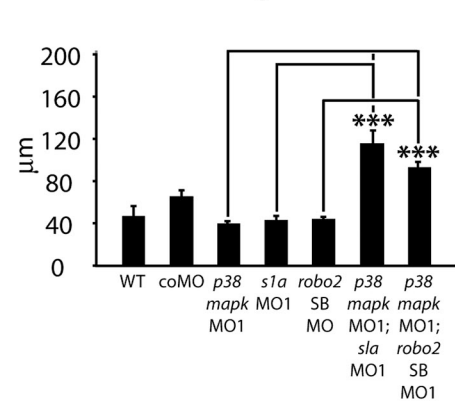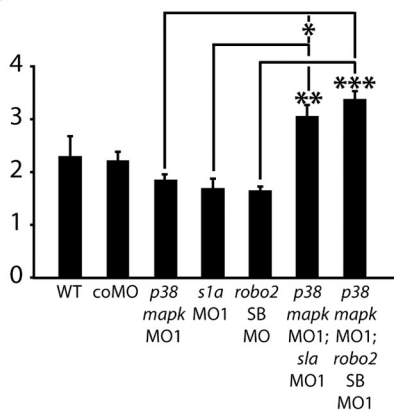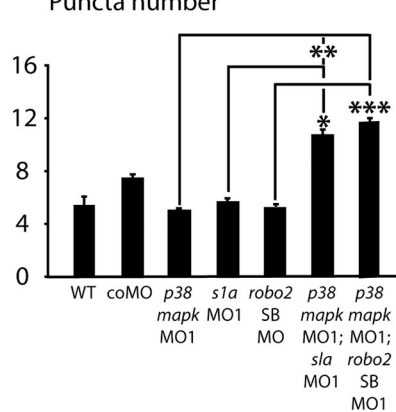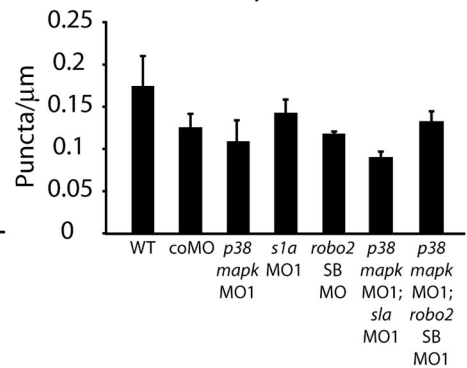
Figure 7. **p38 MAPK interacts with Slit1a-Robo2 signaling to restrict arbor and presynaptic growth.** (A–F) Maximum intensity projections of 80-hpf RGC arbors in the optic tectum expressing YFP-Rab3. coMO (A), *p38mapk*MO1 (B), *slit1a* transMO1 (low dose; C), *robo2*SBMO1 (low dose; D), *p38mapk*MO1; *slit1a* transMO1 (low dose; E), and *p38mapk*MO1; *robo2*SBMO1 (low dose; F). (G–L) Quantification of arbor parameters: branch tip number (G), arbor area (H), total arbor length (I), arbor order (J), presynaptic puncta number (K), and puncta density (L). 6–20 arbors were analyzed per condition. Dorsal views are shown, and anterior is up. White asterisks indicate the parent axon. Error bars represent SEMs. *, $P < 0.05$; **, $P < 0.01$; ***, $P < 0.001$. Bar, 10 µm.

increase in arbor size, complexity, and presynaptic puncta number (Fig. 7, A–F and quantified in G–L). These observations implicate the apoptotic pathway and p38 MAPK as negative regulators of arbor growth via an interaction with Slit1a-Robo2 signaling.

To test for a genetic interaction between *slit1a*, *robo2*, and *casp-3a* in the regulation of branch tip dynamics, we performed time-lapse imaging for 5 h of 80-hpf YFP-Rab3–expressing RGC arbors using combinations of doses of MOs (low dose),

which on their own did not affect arbor dynamics (Fig. 8, A–F and K–M; and Videos 8 and 9). Combining *robo2*SBMO or *slit1a* transMO1 with *casp-3a*MO1 led to a reduction in dynamic and an increase in stable branch tips (Fig. 8, G–J; and Video 10). Significant decreases in branch tip additions and retractions were observed (Fig. 8, K and L), which were accompanied by a significant increase in mean branch tip lifetimes and the proportion of stable branch tips during the 5-h imaging period (Fig. 8, M and N). Furthermore, presynaptic puncta gain and loss were significantly reduced, accompanied by an increase in puncta lifetimes (Fig. 8, O–R). Collectively, these experiments imply a close genetic interaction between Slit1a-Robo2 signaling and the apoptotic pathway in the restriction of arbor, presynaptic growth, and in the promotion of arbor dynamics.

Discussion

A role for the apoptotic pathway in promoting axonal arbor dynamics

We have used a combination of in vivo imaging and genetics and found that the apoptotic pathway promotes axonal arborization and presynaptic dynamics in vivo, which are based on remodeling in terms of branch tip addition and retraction, rather than being physically destructive or degenerative. We identify novel roles for the apoptotic pathway in a local nonapoptotic context, a recently identified cellular phenomenon that is poorly understood. Arbor dynamics occur in response to attractive and repulsive cues enabling pre- and postsynaptic sites to find appropriate partners with which to form stable synapses (Jin and Garner, 2008). The promotion of axonal arbor and presynaptic puncta dynamics indicates that the apoptotic pathway in RGC axonal arbors promotes characteristics of young arbors, rather than maturation as in olfactory neurons (Ohsawa et al., 2010).

Time course of caspase activation

Our study is the first to examine caspase activation in a nonapoptotic role in vivo in the intact living organism. We found that caspase activation occurs rapidly within a 5-min period coinciding with RGC branch point addition in vivo. This is consistent with our earlier in vitro data in which chemotropic cues were able to induce pro–Caspase-3 cleavage and enzymatic activation in 5 min (Campbell and Holt, 2003) and in which cleaved Caspase-3 was detectable after 10 min during the induction of long-term depression (Li et al., 2010). Because SCAT3 can be partially cleaved in vitro by Caspases-8 and -9 (Takemoto et al., 2003), a small proportion of the decrease in FRET observed in RGCs may not be caused by Caspase-3 activation. As the FRET ratio in *casp-3a* morphant RGC arbors is indistinguishable to WT arbors expressing the control uncleavable construct and knockdown of *casp-8* does not affect the FRET ratio (Fig. 1), this possibility is less likely. As SCAT3 is cleaved upon caspase activation and the axonal cytoskeleton may restrict the diffusion of cytoplasmic proteins (Kulkarni et al., 2007), we were unable to fully assess the time course for the activation. Restriction of the diffusion of proteins, such as caspases, in axons could be a mechanism for maintaining their activation locally.

Relationship between caspase activation and upstream regulators

Localization of caspase activity away from the cell body may represent an underlying principle of nonlethal apoptotic pathway activation in neurons, complementing those of lower sublethal and transient caspase activation (Jiao and Li, 2011). The upstream pathways regulating local caspase activation in neurons are largely unknown. We show here that the caspase activation reported by SCAT3 is dependent on Caspase-3, Caspase-9, and p38 MAPK. Because the effect of knockdown of Caspase-3, Caspase-9, and p38 MAPK function on RGC dynamics is similar to the decrease in branch tip and presynaptic puncta dynamics observed in the loss of Slit1a-Robo2 signaling (Campbell et al., 2007), we tested for and identified an interaction between Slit1a-Robo2 signaling, p38 MAPK, and caspase activation and function. In our previous findings that Robo2 acts cell autonomously in RGCs, *slit1a* is strongly expressed in the tectum (Campbell et al., 2007), and here, the fact that caspase activation occurs at the branch points of RGCs suggests a potential model in which Slit1a-induced Robo2 signaling in RGCs via p38 MAPK leads to local apoptotic pathway activation, possibly via localized retention of Slit protein by the extracellular matrix of the tectum (Xiao et al., 2011). The promotion of arbor dynamics and restraining of arbor growth is consistent with preventing the premature maturation of RGC arbors. Other attractive candidates for ligand receptor systems upstream of caspase activation include known activators, such as L-α-lysophosphatidic acid (Steiner et al., 2000; Campbell and Holt, 2003), Sema3A (Shirvan et al., 1999), and Netrin-1 (Campbell and Holt, 2003). Netrin-1 is particularly interesting because it is able to stimulate Caspase-3 activation in vitro (Campbell and Holt, 2003) and promote RGC arbor dynamics in vivo (Manitt et al., 2009), though the relationship between the two remains unexplored.

Knockdown of *casp-9* leading to increased arbor stability is consistent with a role for the intrinsic apoptotic pathway (Ulukaya et al., 2011). This finding is in contrast to our earlier in vitro study (Campbell and Holt, 2003) in which we were unable to identify a role for Caspase-9 in chemotropic turning. A potential reason could be a result of the choice of guidance cues used (Netrin-1 and lysophosphatidic acid; Campbell and Holt, 2003), compared with the interactions of multiple ligand receptor pathways, which could operate in vivo to regulate local caspase activation. The role of other components of the intrinsic pathway, such as mitochondria, present in axons undergoing extensive dynamics (Zinsmaier et al., 2009), remains to be determined. A small proportion of SCAT3 cleavage may be caused by Caspase-9 activity (discussed in the first paragraph of the Discussion), and it remains possible that Caspase-9 also functions independently of Caspase-3. Additionally, Caspases-6 and -8 are present in axons (Carson et al., 2005; Nikolaev et al., 2009), and they may be potentially involved in arbor remodeling independently of Caspases-3 and -9. Furthermore, because very little is known about the presence, localization, and function of the broader caspase family in axons, it remains an open question whether other members may function in arbor remodeling.
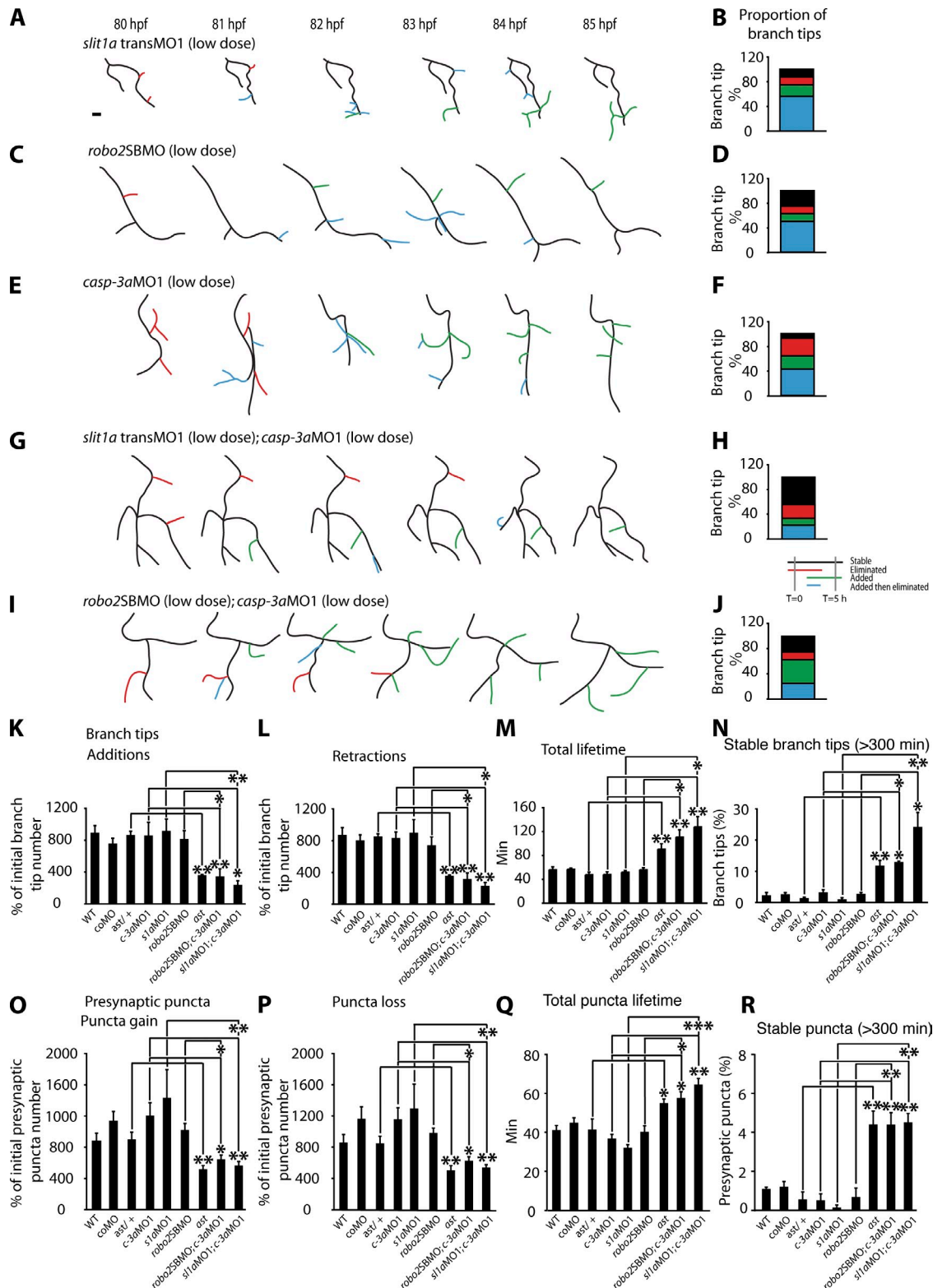
Figure 8. **Caspase-3 interacts with Slit1a-Robo2 signaling to promote arbor dynamics.** (A, C, E, G, and I) Tracings of arbors at 80–85 hpf expressing YFP-Rab3 for *slit1a* transMO1 (low dose; A), *robo2*SBMO (low dose; C), *casp-3a*MO1 (low dose; E), *slit1a* transMO1 (low dose); *casp-3a*MO1 (lose dose; G), and *robo2*SBMO (low dose); *casp-3a*MO1 (low dose; I) morphant arbors every hour during a 5-h time-lapse imaging. Dorsal views are shown. Black, stable branch tips; red, eliminated tips; green, added tips; blue, tips that were added then eliminated during imaging. (B, D, F, H, and J) The proportion of branch tips in each category. These graphs are derived from analysis of a single arbor in a single experiment. (K, L, O, and P) Branch tip additions (K), retractions (L), presynaptic puncta gain (O), and puncta loss (P) are presented as percentages of initial branch tip or puncta number. (M and N) Total branch tip lifetime (M) and the percentage of branch tips present throughout the imaging period (N). (Q and R) Total puncta lifetime (Q) and the percentage of puncta present throughout the imaging period (R). A minimum of five RGC arbors were analyzed per condition. Dorsal views are shown, and anterior is up. Error bars represent SEMs. *, P < 0.05; **, P < 0.01; ***, P < 0.001. Bar, 10 μm.

Possible links to the cytoskeleton and axonal degeneration

Axonal branch tip and presynaptic puncta dynamics are ultimately regulated by the underlying cytoskeleton (Jin and Garner, 2008; Gallo, 2011). Caspase activity regulates cytoskeletal dynamics during apoptotic (Ndozangue-Touriguine et al., 2008) and nonapoptotic processes (Kuranaga et al., 2006; Oshima et al., 2006) and cleaves numerous substrates (Fischer et al., 2003; Timmer and Salvesen, 2007; Crawford and Wells, 2011). Substrates important for axonal arbor remodeling may include actin, actin-binding proteins, and those in signal transduction pathways regulating cytoskeletal dynamics, for example, gelsolin, an actin-severing and -capping protein (Kothakota et al., 1997). Interestingly, cultured hippocampal neurons from gelsolin knockout mice show decreased filopodial dynamics (Lu et al., 1997), reminiscent of the effect of loss of Caspase-3 function on arbor dynamics.

Local apoptotic pathway activation via caspases plays roles in the destructive processes of developmental pruning and axonal degeneration (Kuo et al., 2006; Williams et al., 2006; Nikolaev et al., 2009; Schoenmann et al., 2010; Simon et al., 2012). Our findings that the apoptotic pathway promotes axonal arbor branch tip dynamics may indicate that an optimum amount of or localization of caspase activity is necessary for these nondestructive remodeling processes to occur. Because changes in synaptic function, arbor structure, and axonal degeneration occur early during neurodegenerative conditions, such as Alzheimer's and Parkinson's diseases (Wishart et al., 2006; Saxena and Caroni, 2007; D'Amelio et al., 2011, 2012), identifying the mechanisms of local apoptotic pathway activation in axons may be relevant to understanding these disorders. We propose that the apoptotic pathway is critical for the local remodeling of axonal arbors and presynaptic sites regulating arbor size and shape in the vertebrate CNS.

Materials and methods

Zebrafish embryos

All protocols were reviewed and approved by the Animal Care and Use Committees of the RIKEN Brain Science Institute. WT embryos were obtained by natural matings, raised at 28.5°C, and staged by age and morphology (Kimmel et al., 1995). WT embryos were obtained from RIKEN WT, tupfel longfin (TL), and AB strains. TL's were provided by the Zebrafish International Resource Center (which is supported by grant P40 RR012546 from the National Institutes of Health–National Center for Research Resources) and by H. Baier and K. Slanchez of the Max Planck Institute for Neurobiology, Martinsried, Germany. *ast^{ti272z}* (*ast*)/*robo2* mutant embryos were obtained by crosses of homozygous mutants, provided by C.-B. Chien and M.-Y. Law (University of Utah, Salt Lake City, UT), and *ast^{ti272z}*/+ was generated by crossing to RIKEN WT or TL strains.

In situ hybridization

In situ hybridization was performed as described using digoxigenin-labeled antisense probes (Schulte-Merker et al., 1992; Lee et al., 2001) of *casp-3a* (a gift from M. Yamashita, National Research Institute of Fisheries Science, Yokohama, Japan; Yabu et al., 2001), *casp-8* (GenBank accession no. BC081583; clone ID 2351947 obtained from Thermo Fisher Scientific; Eimon et al., 2006), and *casp-9* (GenBank accession no. BC085434; obtained from the zebrafish gene collection, clone ID 7226798; Thermo Fisher Scientific) on 80-hpf embryos. Embryos were fixed in 4% PFA for 2 h at RT or overnight at 4°C followed by a graded methanol series to 100% methanol overnight at −20°C. Embryos were rehydrated via a graded methanol series and washed 3× for 5 min in PBST (PBS and Tween) followed by treatment with 0.1%

collagenase for 50 min at RT. Embryos were then washed 3× for 5 min in PBST at RT followed by after fixation in 4% PFA for 20 min and washed for 3× for 5 min in PBST before incubation for 60 min at RT with 2.5 µl/ml acetic anhydride in 0.1 M triethanolamine. Embryos were washed for 2× for 10 min in PBST. Embryos were prehybridized for ∼2 h at 65°C followed by hybridization with probe at 1:50 or 1:100 dilutions overnight at 65°C. Incubation with 10 µg/ml RNaseA for 30 min at 65°C and two SSCT (SSC and Tween) washes. Reuse of sense and antisense probes helped to improve the signal to noise ratios. After probe hybridization and removal, embryos were washed 2× in 50% formamide and 2× SSCT for 30 min at 65°C followed by 2× for 30 min each in 2× and 0.2× SSCT. Embryos were incubated 1–5 h with 2% blocking reagent (Roche) in maleic acid buffer before being incubated overnight at RT with a 1:5,000 dilution of antidigoxigenin alkaline phosphatase Fab fragments (Roche) in 2% blocking reagent. Unbound Fab fragments were removed with washes for 25 min in 2% blocking reagent and 3× for 25 min in maleic acid buffer followed by incubation in BM purple (Roche) for colorimetric staining. The color reaction was stopped by 3 × 5–min PBST washes followed by fixation in 4% PFA for 2 h at RT and transfer to 100% methanol as described earlier in this paragraph. After rehydration in PBST, clearing of the embryos was performed through a graded glycerol series to 70% glycerol and stored at 4°C before imaging. Whole-mount in situ hybridized embryos were embedded in agarose in PBS, fixed in 4% PFA, sectioned at 60 µm on a vibratome (DSK Microslicer DTK-3000W; Ted Pella), coverslipped in 80% glycerol, imaged, and photographed using a microscope (Axioplan 2; Carl Zeiss) with a 40× Achroplan, NA 0.65 or 20× Achroplan, NA 0.5, a camera (AxioCam HRc; Carl Zeiss), and Axiovision (Carl Zeiss) or MetaMorph (Molecular Devices) software.

DNA constructs and MO antisense oligonucleotides

Constructs used in this study were as follows: *isl2b* (*islet2b*):*GAL4VP16* (originally named *islet3:GAL4VP16*; Campbell et al., 2007), the zebrafish *islet3* gene was renamed *isl2b* (Pittman et al., 2008), *UAS:SCAT3* and *UAS: SCAT3DEVG* (control; gifts from M. Miura and Y. Yamaguchi, The University of Tokyo, Bunkyo, Tokyo, Japan; Takemoto et al., 2003, 2007), and *UAS: YFP-Rab3* (Campbell et al., 2007). The following MO antisense oligonucleotides were obtained from Gene Tools: *casp-3a*MO1, 5′-TTGCGTCCACA-CACAGTCTCCGTTCAT-3′, which has been shown to be effective in zebrafish (Yamashita et al., 2008); *casp-9*MO1, 5′-GAATCTGTCTGT-GTTTCTGCTCCAT-3′; *casp-9*SBMO1 (Sidi et al., 2008), 5′-GATGGAAAAA-CACACTTACGGACTG-3′; control (coMO; five–base pair mismatch for *casp-3a*MO1; lower cases letters represent the base changes), 5′-TTcCGTa-CACAgAGTCTCCcTTgAT-3′; *slit1a* transMO1, 5′-GACAACATCCTCCTCTC-GCAGGCAT-3′ (Barresi et al., 2005; Campbell et al., 2007); *robo2*SBMO, 5′-TAAAAAGTAGCGCAACTCACCATCC-3′ (Wyatt et al., 2010); *casp-8*MO1, 5′-ACAGGGTTTTAACTCACAGTAGATC-3′ (Sidi et al., 2008); and *p38mapk*MO1, 5′-AGTGGGTCTTTCTTTCTGCGACATG-3′ (Hsu et al., 2011). *robo2*SBMO and *slit1a* transMO1 were injected at 2- or 1-ng/nl doses, respectively, which did not affect overall arbor growth on their own, except for the *slit1a* transMO1 experiments described in Fig. 5 (E–H) in which 2 ng MO was injected, which increases arbor size and complexity (Campbell et al., 2007). For the epistasis experiments examining arbor dynamics in Fig. 8, combinations of doses of MOs were used that on their own did not affect arbor dynamics (*slit1a* transMO1 [low dose, 1 ng], *robo2*SBMO [low dose, 2 ng], and *casp-3a*MO1 [low dose, 0.5 ng]). MOs were diluted (combined with DNA constructs) and injected to a final volume of ∼1 nl, being one fifth the size of the yolk, into one- to four-cell stage embryos. MOs against the target genes are effective in zebrafish, and because high doses of *casp-3a*MO1, *casp-8*MO1, *casp-9*MO1, *casp-9*SBMO1, *slit1a* transMO1, *robo2*SBMO, and *p38mapk*MO1 can generate morphological phenotypes, the doses were chosen to avoid these and represent a partial loss of function (Campbell et al., 2007; Sidi et al., 2008; Yamashita et al., 2008; Wyatt et al., 2010; Hsu et al., 2011).

Labeling of RGCs and tectal cells

Single RGCs or tectal cells were labeled by mosaic expression after coinjection into one to four cell embryos of the plasmids *isl2b:GAL4VP16* and *UAS: SCAT3*, *UAS:SCAT3DEVG* (control), or *UAS:YFP-Rab3*. Embryos were screened at ∼76 hpf for one or a few RGC axonal arbors in the caudomedial region of the optic tectum. This area is relatively flat, in the center of the tectum and where RGC arbors are close to the surface of the brain, avoiding the likelihood of being obscured by the autofluorescence of the skin (Hutson et al., 2004; Campbell et al., 2007). Arbors that overlapped with or were in close proximity to other arbors, making it difficult to distinguish individual arbors, were eliminated from our analyses. RGC cell bodies for imaging were located in the central retina. Tectal cell bodies for imaging were located in

the periventricular region of the optic tectum, close to the surface of the brain. Because SCAT3 or control construct expression level varied and to minimize any effects as a result of arbor morphology or movement on the FRET ratio between RGC arbors, we examined a broad population (19–28) of arbors per condition and observed consistent differences in the Venus/ECFP ratio between SCAT3 and control constructs. The effect of expression levels on the Venus/ECFP ratio appeared minimal. WT- and SCAT3-expressing RGC arbors were indistinguishable in arbor size and branch tip dynamics from those expressing YFP-Rab3. Arbor parameters were as follows: branch tip number, WT YFP-Rab3 4.2 ± 0.67 compared with SCAT3 4.086 ± 0.39 (P > 0.1); arbor area, WT YFP-Rab3 150.60 ± 39.70 µm² compared with SCAT3 157.73 ± 7.45 µm² (P > 0.1); and total arbor length, WT YFP-Rab3 46.64 ± 10.08 µm compared with SCAT3 45.26 ± 1.90 µm (P > 0.1). Arbor dynamics were as follows: branch tip additions, WT YFP-Rab3 737.19 ± 65.2% compared with SCAT3 793.5 ± 96.14% (P > 0.1); branch tip retractions, WT YFP-Rab3 752.57 ± 131% compared with SCAT3 778.74 ± 131.79% (P > 0.1); and mean total branch tip lifetimes, WT YFP-Rab3 55.86 ± 5.3 min compared with SCAT3 54.95 ± 4.01% (P > 0.1).

SCAT3 reporter imaging of RGCs and tectal cells and image analysis

Imaging of RGCs or tectal cells expressing SCAT3 or control constructs was performed using a confocal microscope (FV1000D [Olympus] or LSM 780 [Carl Zeiss]). Embryos were restrained by anaesthetization in 0.004% tricaine and mounted dorsal side down in 1.5% low melting point agarose (NuSieve; Lonza) in a Lab-Tek two-chambered #1.0 borosilicate coverglass system (Thermo Fisher Scientific). Imaging was performed using 440- or 458-nm laser excitation with 60× U Plan S Apochromat, NA 1.2 water, 60× U Plan S Apochromat, NA 1.3 silicone oil, or 63× C-Apochromat, NA 1.2 water objectives. Emission was detected at 460–500 nm (ECFP) and 515–615 nm (Venus). 10–30 1- or 2-µm z stacks were collected (512 × 512 pixels). Care was taken to avoid pixel saturation. For time-lapse imaging with SCAT3, z stacks were collected every 5 min for ∼2 h at ∼26°C. The viability of the embryos was confirmed with a beating heart and blood flow after the imaging period. Only samples with minimum movement (where movement was not observed on images during confocal laser scanning) were analyzed, and individual time points were treated independently with their own internal reference of, for example, background fluorescence as described in the next paragraph. Stacks were aligned to eliminate x-y drift using the StackReg plugin in ImageJ (National Institutes of Health).

　　　Images were analyzed as maximum intensity z projections of the ECFP and Venus channels using ImageJ software. A stack of the Venus and ECFP z projections was created to precisely align the images. Venus/ECFP ratios over the whole RGC arbor or tectal cell body were determined using the polygon selection tool at a zoom of 200% to trace around all the branch tips and intermodal regions of the arbor to the branch point closest to the parent axon or cell body on the Venus channel followed by calculating the mean fluorescence intensity per unit area for both the Venus and ECFP channels. Mean background fluorescence intensity from identical regions of each channel was subtracted from the mean fluorescence intensity measurements, the ratio calculated and expressed as a percentage of Venus/ECFP. Background-subtracted Venus/ECFP ratios at branch points and surrounding regions were calculated as earlier in this paragraph except using the polygon selection tool to trace around branch points and three surrounding regions on the same arbor, adjacent to the branch point as described in Fig. 1 (B–D and F–H). The mean Venus/ECFP ratio of the three surrounding regions is depicted in the graphs (Figs. 1 T, 2 F, and 5 G). Representative intensity modulated display (IMD) images were generated using the ratio images function in MetaMorph software. Measurement of arbor parameters on the YFP and IMD ratio images was very similar, showing that the whole of the arbor is visible in the ratio images (Fig. S2, A–D). Images presented in Figs. 1, 2, 3, 5, 6, 7, S3, S4, and S5 and Videos 1, 2, 3, 4, 5, 6, 7, 8, 9, and 10 were median filtered (radius of 1 pixel) to reduce noise, and input levels were set to 100 or 150 to increase brightness for displaying. Time indicators were added to the Videos 1, 2, 3, 4, 5, 6, 7, 8, 9, and 10 using the Time Stamper function, and arrowheads in Video 1 were added with the Arrow Maker Tool plugin in ImageJ.

Branch tip and presynaptic puncta time-lapse imaging and image analysis

Imaging of arbors expressing YFP-Rab3 was performed using an upright (LSM 510 META; Carl Zeiss), inverted (LSM 780), or an upright confocal microscope (FV1000D) as described previously (Campbell et al., 2007). YFP-Rab3 was excited with 515- or 514-nm laser lines, and emission was detected with a 530–600-nm band pass filter or a BA535–564-nm barrier

filter. 10–35 2.0-µm z stacks (512 × 512 pixels) were collected every 15 min for 5 h, incubated at 26°C with a 63× N-Achroplan, NA 0.9 long working distance water immersion objective on the LSM 510 META, a 63× C-Apochromat, NA 1.2 objective on the LSM 780, or a 60× LUMPFL, NA 0.9 long working distance water immersion objective on the FV1000D. Care was taken to avoid pixel saturation. The viability of the embryos was verified after imaging via confirmation of a beating heart and blood flow. Time-lapse images were processed using the group z projector plugin for ImageJ, and individual images were saved as an 8-bit TIFF stack. Because YFP-Rab3 is trafficked to both synaptic and nonsynaptic membrane compartments, it is possible to use it to view both presynaptic sites and axonal arbor morphology. Branch tip tracking was performed on unthresholded images. The numbers and lifetimes of YFP-Rab3–expressing presynaptic sites were quantified using thresholding in ImageJ software. A YFP-Rab3 punctum was defined as an area of ≥2 pixels whose intensity was ≥5× that of a nonpunctate region of the same arbor and saved as an 8-bit TIFF stack (Campbell et al., 2007). The fluorescence intensity of each arbor was normalized to a nonpunctate region of the same arbor, i.e., the parent axon. Tracking of branch tips and presynaptic puncta through different time points was performed manually using the ObjectJ for ImageJ plugin written by N. Vischer (University of Amsterdam, Amsterdam, Netherlands); source code can be found in Supplemental material). Total branch tip and presynaptic puncta lifetimes were defined as a branch tip or presynaptic punctum being present in one or more time-lapse imaging frames, calculated by summing up the number of frames that either was present for, and multiplied by 15 (the duration between frames) to generate the lifetime in minutes.

Quantification of arbor parameters

Maximum intensity projections of YFP-Rab3–expressing arbors were quantified as in Campbell et al. (2007): The number of branch tips >4 µm are counted. The total arbor length is the sum of all branch tip lengths and internodal distances. The arbor area is defined by a convex polygon joining all branch tips. The order of an arbor is the mean number of branch points counted between a branch tip and the first branch point of the arbor. For puncta number, images were thresholded as in the preceding paragraph and counted using the analyze particle function with a pixel size of >2 in ImageJ software.

Caspase-3 activation of SCAT3

Tectal cell bodies of 76–80-hpf zebrafish larvae expressing SCAT3 or control construct (control) in one or a few tectal cells were imaged on an inverted FV1000D confocal microscope as described in the section SCAT3 reporter imaging of RGCs and tectal cells and image analysis. After imaging, embryos were remounted (dorsal up) in 1.5% low melting point agarose (NuSieve) on a glass microscope slide. The Caspase-3 activator PAC-1 (procaspase-activating compound 1; Tocris Bioscience; Putt et al., 2006) was dissolved in DMSO followed by embryo medium to a final concentration of 40 µm and pressure injected into the tectal ventricle, an approach previously shown to be able to target reagents to tectal cells (Leu and Schmidt, 2008). Embryos were placed individually in 500 µl embryo medium in a 24-well plate and incubated at RT for 3 h, sufficient time for PAC-1 to induce a high proportion of TUNEL-positive apoptotic cells in the retina and tectum (described in the next section). Embryos were subsequently remounted for an inverted confocal microscope (FV1000D), and imaging and analysis were performed as described earlier in this paragraph.

TUNEL labeling

TUNEL labeling was performed using the In Situ Cell Death Detection kit, polymerized horse radish peroxidase (Roche). 80-hpf embryos were fixed in 4% PFA and permeabilized with 100% methanol at −20°C followed by 0.1% collagenase at RT and PBST washes. Samples were incubated in TUNEL reaction mixture for 60 min at 37°C in the dark. After PBST washes, samples were incubated with antifluorescein–polymerized horse radish peroxidase (Roche) at a dilution of 1:1,000 overnight, washed in PBST, and stained with 0.5 mg/ml 3,3-diaminobenzidine with 0.0003% H_2O_2 in PBST.

　　　Embryos were mounted in 70% glycerol and placed in a glass plate and imaged using a stereo dissecting microscope (SZX16; Olympus) with a super depth of focus Plan Apochromat 1× parfocal objective zoom 5 and a camera (DP50-CU; Olympus) at 1,392 × 1,040 pixels with Studio Lite software (Olympus). Preincubation with 20 µm of the Bcl-2 (B cell lymphoma 2) inhibitor HA14-1 (Sigma-Aldrich) for 1 h was used as a positive control for TUNEL labeling.

Acceptor photobleaching of SCAT3

To test for the presence of FRET between the ECFP and Venus moieties of SCAT3 and the uncleavable control construct (control), 80-hpf RGC arbors

and tectal cell bodies were imaged before and after partial photobleaching by exposure to 100% laser power of a 514-nm laser line from a multi-argon line laser (Melles Griot) for 5 min. Reimaging of the Venus/ECFP ratios of the same cells was performed as described in the section SCAT3 reporter imaging of RGCs and tectal cells and image analysis.

Imaging RGC pathfinding to the optic tectum

For lateral views, embryos with YFP-Rab3–labeled RGC axons were processed for anti-GFP immunohistochemistry. Approximately 80-hpf embryos were fixed and permeabilized as described for in situ hybridization. After the collagenase PBST washes, embryos were blocked in 10% fetal calf serum for 1 h at RT followed by incubation overnight at 4°C with a chicken primary anti-GFP polyclonal antibody (Aves Labs, Inc.) at a dilution of 1:3,000. The primary antibody was washed off with 4 × 30–min washes in PBST at RT followed by incubation for 4 h with an anti–chicken Alexa Fluor 488–conjugated secondary antibody (Molecular Probes and Invitrogen), diluted 1:500. After 4 × 30–min PBST washes, embryos were mounted in 1.5% low melting point agarose for an upright confocal microscope (510 META). Images were captured as a z series (step sizes of 2 µm) of 513 × 512–pixel scans using a long working distance 20×, NA 0.5 N-Achroplan water immersion objective and a digital zoom of 0.8.

Statistical analyses

Statistical analyses were performed using Prism version 4 software (GraphPad Software). As it can be difficult to determine accurately whether datasets follow a normal Gaussian distribution or not, we applied nonparametric statistical analyses, which are usually more stringent, using the Mann–Whitney U test, allowing for whether standard deviations of the conditions being compared were significantly different when comparing two conditions. When comparing three or more conditions, the Kruskal–Wallace test with a post hoc Dunn's multiple comparison test was used. $P < 0.05$ was considered statistically significant. All results are presented as mean values ± SEM.

Online supplemental material

Fig. S1 shows caspases are expressed in RGCs and the tectum. Fig. S2 shows that SCAT3 reports Caspase-3 activation. Fig. S3 shows caspase activation is undetectable in tectal dendrites. Fig. S4 shows caspase activation remains lower after branch tip retraction. Fig. S5 shows that in caspase morphants, RGC axons follow normal paths to the optic tectum. Video 1 shows the dynamics of caspase activity in young RGC arbors. Video 2 shows the dynamics of caspase activation in older arbors. Video 3 shows that WT arbors are highly dynamic. Video 4 shows that coMO arbors are highly dynamic. Video 5 shows that *casp-3a* knockdown leads to more stable arbors. Video 6 shows that *casp-9* knockdown leads to more stable arbors. Video 7 shows that *p38mapk* knockdown leads to more stable arbors. Video 8 shows that low dose MO against *casp-3a* does not affect arbor dynamics. Video 9 shows that low dose MO against *slit1a* does not affect arbor dynamics. Video 10 shows that a combination of low dose *casp-3a*MO1 and low dose *slit1a* transMO1 leads to more stable arbors. A source code for ObjectJ plugin for ImageJ is also provided in a ZIP file (containing source code objectj_-o.96d.jar, branch macro branches-2.txt, branches object file Branches-2.ojj, and a demo file demo-1.tiff). Online supplemental material is available at http://www.jcb.org/cgi/content/full/jcb.201303072/DC1.

References

Alsina, B., T. Vu, and S. Cohen-Cory. 2001. Visualizing synapse formation in arborizing optic axons in vivo: dynamics and modulation by BDNF. *Nat. Neurosci.* 4:1093–1101. http://dx.doi.org/10.1038/nn735

Barresi, M.J., L.D. Hutson, C.B. Chien, and R.O. Karlstrom. 2005. Hedgehog regulated Slit expression determines commissure and glial cell position in the zebrafish forebrain. *Development.* 132:3643–3656. http://dx.doi.org/10.1242/dev.01929

Bashaw, G.J., and R. Klein. 2010. Signaling from axon guidance receptors. *Cold Spring Harb. Perspect. Biol.* 2:a001941. http://dx.doi.org/10.1101/cshperspect.a001941

Biehlmaier, O., S.C. Neuhauss, and K. Kohler. 2001. Onset and time course of apoptosis in the developing zebrafish retina. *Cell Tissue Res.* 306:199–207. http://dx.doi.org/10.1007/s004410100447

Bingol, B., and M. Sheng. 2011. Deconstruction for reconstruction: the role of proteolysis in neural plasticity and disease. *Neuron.* 69:22–32. http://dx.doi.org/10.1016/j.neuron.2010.11.006

Cajigas, I.J., T. Will, and E.M. Schuman. 2010. Protein homeostasis and synaptic plasticity. *EMBO J.* 29:2746–2752. http://dx.doi.org/10.1038/emboj.2010.173

Campbell, D.S., and C.E. Holt. 2001. Chemotropic responses of retinal growth cones mediated by rapid local protein synthesis and degradation. *Neuron.* 32:1013–1026. http://dx.doi.org/10.1016/S0896-6273(01)00551-7

Campbell, D.S., and C.E. Holt. 2003. Apoptotic pathway and MAPKs differentially regulate chemotropic responses of retinal growth cones. *Neuron.* 37:939–952. http://dx.doi.org/10.1016/S0896-6273(03)00158-2

Campbell, D.S., A.G. Regan, J.S. Lopez, D. Tannahill, W.A. Harris, and C.E. Holt. 2001. Semaphorin 3A elicits stage-dependent collapse, turning, and branching in *Xenopus* retinal growth cones. *J. Neurosci.* 21:8538–8547.

Campbell, D.S., S.A. Stringham, A. Timm, T. Xiao, M.Y. Law, H. Baier, M.L. Nonet, and C.B. Chien. 2007. Slit1a inhibits retinal ganglion cell arborization and synaptogenesis via Robo2-dependent and -independent pathways. *Neuron.* 55:231–245. http://dx.doi.org/10.1016/j.neuron.2007.06.034

Carson, C., M. Saleh, F.W. Fung, D.W. Nicholson, and A.J. Roskams. 2005. Axonal dynactin p150Glued transports caspase-8 to drive retrograde olfactory receptor neuron apoptosis. *J. Neurosci.* 25:6092–6104. http://dx.doi.org/10.1523/JNEUROSCI.0707-05.2005

Cohen-Cory, S. 2007. Imaging retinotectal synaptic connectivity. *CSH Protoc.* 2007:pdb.prot4782. http://dx.doi.org/10.1101/pdb.prot4782

Cohen-Cory, S., and S.E. Fraser. 1995. Effects of brain-derived neurotrophic factor on optic axon branching and remodelling in vivo. *Nature.* 378:192–196. http://dx.doi.org/10.1038/378192a0

Crawford, E.D., and J.A. Wells. 2011. Caspase substrates and cellular remodeling. *Annu. Rev. Biochem.* 80:1055–1087. http://dx.doi.org/10.1146/annurev-biochem-061809-121639

Creagh, E.M., and S.J. Martin. 2001. Caspases: cellular demolition experts. *Biochem. Soc. Trans.* 29:696–702. http://dx.doi.org/10.1042/BST0290696

D'Amelio, M., V. Cavallucci, S. Middei, C. Marchetti, S. Pacioni, A. Ferri, A. Diamantini, D. De Zio, P. Carrara, L. Battistini, et al. 2011. Caspase-3 triggers early synaptic dysfunction in a mouse model of Alzheimer's disease. *Nat. Neurosci.* 14:69–76. http://dx.doi.org/10.1038/nn.2709

D'Amelio, M., M. Sheng, and F. Cecconi. 2012. Caspase-3 in the central nervous system: beyond apoptosis. *Trends Neurosci.* 35:700–709. http://dx.doi.org/10.1016/j.tins.2012.06.004

Dingwell, K.S., C.E. Holt, and W.A. Harris. 2000. The multiple decisions made by growth cones of RGCs as they navigate from the retina to the tectum in *Xenopus* embryos. *J. Neurobiol.* 44:246–259. http://dx.doi.org/10.1002/1097-4695(200008)44:2<246::AID-NEU13>3.0.CO;2-K

Eimon, P.M., E. Kratz, E. Varfolomeev, S.G. Hymowitz, H. Stern, J. Zha, and A. Ashkenazi. 2006. Delineation of the cell-extrinsic apoptosis pathway in the zebrafish. *Cell Death Differ.* 13:1619–1630. http://dx.doi.org/10.1038/sj.cdd.4402015

Fischer, U., R.U. Jänicke, and K. Schulze-Osthoff. 2003. Many cuts to ruin: a comprehensive update of caspase substrates. *Cell Death Differ.* 10:76–100. http://dx.doi.org/10.1038/sj.cdd.4401160

Gallo, G. 2011. The cytoskeletal and signaling mechanisms of axon collateral branching. *Dev. Neurobiol.* 71:201–220. http://dx.doi.org/10.1002/dneu.20852

Gibson, D.A., and L. Ma. 2011. Developmental regulation of axon branching in the vertebrate nervous system. *Development*. 138:183–195. http://dx.doi.org/10.1242/dev.046441

Harris, W.A., C.E. Holt, and F. Bonhoeffer. 1987. Retinal axons with and without their somata, growing to and arborizing in the tectum of *Xenopus* embryos: a time-lapse video study of single fibres in vivo. *Development*. 101:123–133.

Hsu, R.J., C.C. Lin, Y.F. Su, and H.J. Tsai. 2011. dickkopf-3-related gene regulates the expression of zebrafish myf5 gene through phosphorylated p38a-dependent Smad4 activity. *J. Biol. Chem.* 286:6855–6864. http://dx.doi.org/10.1074/jbc.M110.161638

Huesmann, G.R., and D.F. Clayton. 2006. Dynamic role of postsynaptic caspase-3 and BIRC4 in zebra finch song-response habituation. *Neuron*. 52:1061–1072. http://dx.doi.org/10.1016/j.neuron.2006.10.033

Hutson, L.D., D.S. Campbell, and C.B. Chien. 2004. Analyzing axon guidance in the zebrafish retinotectal system. *Methods Cell Biol.* 76:13–35. http://dx.doi.org/10.1016/S0091-679X(04)76002-1

Hyman, B.T., and J. Yuan. 2012. Apoptotic and non-apoptotic roles of caspases in neuronal physiology and pathophysiology. *Nat. Rev. Neurosci.* 13:395–406. http://dx.doi.org/10.1038/nrn3228

Jiao, S., and Z. Li. 2011. Nonapoptotic function of BAD and BAX in long-term depression of synaptic transmission. *Neuron*. 70:758–772. http://dx.doi.org/10.1016/j.neuron.2011.04.004

Jin, Y., and C.C. Garner. 2008. Molecular mechanisms of presynaptic differentiation. *Annu. Rev. Cell Dev. Biol.* 24:237–262. http://dx.doi.org/10.1146/annurev.cellbio.23.090506.123417

Jung, H., C.M. O'Hare, and C.E. Holt. 2011. Translational regulation in growth cones. *Curr. Opin. Genet. Dev.* 21:458–464. http://dx.doi.org/10.1016/j.gde.2011.04.004

Kimmel, C.B., W.W. Ballard, S.R. Kimmel, B. Ullmann, and T.F. Schilling. 1995. Stages of embryonic development of the zebrafish. *Dev. Dyn.* 203:253–310. http://dx.doi.org/10.1002/aja.1002030302

Kothakota, S., T. Azuma, C. Reinhard, A. Klippel, J. Tang, K. Chu, T.J. McGarry, M.W. Kirschner, K. Koths, D.J. Kwiatkowski, and L.T. Williams. 1997. Caspase-3-generated fragment of gelsolin: effector of morphological change in apoptosis. *Science*. 278:294–298. http://dx.doi.org/10.1126/science.278.5336.294

Krens, S.F., S. He, H.P. Spaink, and B.E. Snaar-Jagalska. 2006. Characterization and expression patterns of the MAPK family in zebrafish. *Gene Expr. Patterns*. 6:1019–1026. http://dx.doi.org/10.1016/j.modgep.2006.04.008

Kulkarni, R.P., M. Bak-Maier, and S.E. Fraser. 2007. Differences in protein mobility between pioneer versus follower growth cones. *Proc. Natl. Acad. Sci. USA*. 104:1207–1212. http://dx.doi.org/10.1073/pnas.0610142104

Kuo, C.T., S. Zhu, S. Younger, L.Y. Jan, and Y.N. Jan. 2006. Identification of E2/E3 ubiquitinating enzymes and caspase activity regulating *Drosophila* sensory neuron dendrite pruning. *Neuron*. 51:283–290. http://dx.doi.org/10.1016/j.neuron.2006.07.014

Kuranaga, E., and M. Miura. 2007. Nonapoptotic functions of caspases: caspases as regulatory molecules for immunity and cell-fate determination. *Trends Cell Biol.* 17:135–144. http://dx.doi.org/10.1016/j.tcb.2007.01.001

Kuranaga, E., H. Kanuka, A. Tonoki, K. Takemoto, T. Tomioka, M. Kobayashi, S. Hayashi, and M. Miura. 2006. *Drosophila* IKK-related kinase regulates nonapoptotic function of caspases via degradation of IAPs. *Cell*. 126:583–596. http://dx.doi.org/10.1016/j.cell.2006.05.048

Lee, J.S., R. Ray, and C.B. Chien. 2001. Cloning and expression of three zebrafish roundabout homologs suggest roles in axon guidance and cell migration. *Dev. Dyn.* 221:216–230. http://dx.doi.org/10.1002/dvdy.1136

Leu, B.H., and J.T. Schmidt. 2008. Arachidonic acid as a retrograde signal controlling growth and dynamics of retinotectal arbors. *Dev. Neurobiol.* 68:18–30. http://dx.doi.org/10.1002/dneu.20561

Li, Z., J. Jo, J.M. Jia, S.C. Lo, D.J. Whitcomb, S. Jiao, K. Cho, and M. Sheng. 2010. Caspase-3 activation via mitochondria is required for long-term depression and AMPA receptor internalization. *Cell*. 141:859–871. http://dx.doi.org/10.1016/j.cell.2010.03.053

Lin, Y.C., and A.J. Koleske. 2010. Mechanisms of synapse and dendrite maintenance and their disruption in psychiatric and neurodegenerative disorders. *Annu. Rev. Neurosci.* 33:349–378. http://dx.doi.org/10.1146/annurev-neuro-060909-153204

Lu, M., W. Witke, D.J. Kwiatkowski, and K.S. Kosik. 1997. Delayed retraction of filopodia in gelsolin null mice. *J. Cell Biol.* 138:1279–1287. http://dx.doi.org/10.1083/jcb.138.6.1279

Manitt, C., A.M. Nikolakopoulou, D.R. Almario, S.A. Nguyen, and S. Cohen-Cory. 2009. Netrin participates in the development of retinotectal synaptic connectivity by modulating axon arborization and synapse formation in the developing brain. *J. Neurosci.* 29:11065–11077. http://dx.doi.org/10.1523/JNEUROSCI.0947-09.2009

Meyer, M.P., and S.J. Smith. 2006. Evidence from in vivo imaging that synaptogenesis guides the growth and branching of axonal arbors by two distinct mechanisms. *J. Neurosci.* 26:3604–3614. http://dx.doi.org/10.1523/JNEUROSCI.0223-06.2006

Ming, G.L., S.T. Wong, J. Henley, X.B. Yuan, H.J. Song, N.C. Spitzer, and M.M. Poo. 2002. Adaptation in the chemotactic guidance of nerve growth cones. *Nature*. 417:411–418. http://dx.doi.org/10.1038/nature745

Ndozangue-Touriguine, O., J. Hamelin, and J. Bréard. 2008. Cytoskeleton and apoptosis. *Biochem. Pharmacol.* 76:11–18. http://dx.doi.org/10.1016/j.bcp.2008.03.016

Nikolaev, A., T. McLaughlin, D.D. O'Leary, and M. Tessier-Lavigne. 2009. APP binds DR6 to trigger axon pruning and neuron death via distinct caspases. *Nature*. 457:981–989. http://dx.doi.org/10.1038/nature07767

O'Donnell, M., R.K. Chance, and G.J. Bashaw. 2009. Axon growth and guidance: receptor regulation and signal transduction. *Annu. Rev. Neurosci.* 32:383–412. http://dx.doi.org/10.1146/annurev.neuro.051508.135614

Ohsawa, S., S. Hamada, K. Kuida, H. Yoshida, T. Igaki, and M. Miura. 2010. Maturation of the olfactory sensory neurons by Apaf-1/caspase-9-mediated caspase activity. *Proc. Natl. Acad. Sci. USA*. 107:13366–13371. http://dx.doi.org/10.1073/pnas.0910488107

Oshima, K., M. Takeda, E. Kuranaga, R. Ueda, T. Aigaki, M. Miura, and S. Hayashi. 2006. IKK epsilon regulates F actin assembly and interacts with *Drosophila* IAP1 in cellular morphogenesis. *Curr. Biol.* 16:1531–1537. http://dx.doi.org/10.1016/j.cub.2006.06.032

Pittman, A.J., M.Y. Law, and C.B. Chien. 2008. Pathfinding in a large vertebrate axon tract: isotypic interactions guide retinotectal axons at multiple choice points. *Development*. 135:2865–2871. http://dx.doi.org/10.1242/dev.025049

Poulain, F.E., J.A. Gaynes, C. Stacher Hörndli, M.Y. Law, and C.B. Chien. 2010. Analyzing retinal axon guidance in zebrafish. *Methods Cell Biol.* 100:3–26.

Putt, K.S., G.W. Chen, J.M. Pearson, J.S. Sandhorst, M.S. Hoagland, J.T. Kwon, S.K. Hwang, H. Jin, M.I. Churchwell, M.H. Cho, et al. 2006. Small-molecule activation of procaspase-3 to caspase-3 as a personalized anticancer strategy. *Nat. Chem. Biol.* 2:543–550. http://dx.doi.org/10.1038/nchembio814

Ruthazer, E.S., J. Li, and H.T. Cline. 2006. Stabilization of axon branch dynamics by synaptic maturation. *J. Neurosci.* 26:3594–3603. http://dx.doi.org/10.1523/JNEUROSCI.0069-06.2006

Sato, T., T. Hamaoka, H. Aizawa, T. Hosoya, and H. Okamoto. 2007. Genetic single-cell mosaic analysis implicates ephrinB2 reverse signaling in projections from the posterior tectum to the hindbrain in zebrafish. *J. Neurosci.* 27:5271–5279. http://dx.doi.org/10.1523/JNEUROSCI.0883-07.2007

Saxena, S., and P. Caroni. 2007. Mechanisms of axon degeneration: from development to disease. *Prog. Neurobiol.* 83:174–191. http://dx.doi.org/10.1016/j.pneurobio.2007.07.007

Schoenmann, Z., E. Assa-Kunik, S. Tiomny, A. Minis, L. Haklai-Topper, E. Arama, and A. Yaron. 2010. Axonal degeneration is regulated by the apoptotic machinery or a NAD+-sensitive pathway in insects and mammals. *J. Neurosci.* 30:6375–6386. http://dx.doi.org/10.1523/JNEUROSCI.0922-10.2010

Schulte-Merker, S., R.K. Ho, B.G. Herrmann, and C. Nüsslein-Volhard. 1992. The protein product of the zebrafish homologue of the mouse T gene is expressed in nuclei of the germ ring and the notochord of the early embryo. *Development*. 116:1021–1032.

Shirvan, A., I. Ziv, G. Fleminger, R. Shina, Z. He, I. Brudo, E. Melamed, and A. Barzilai. 1999. Semaphorins as mediators of neuronal apoptosis. *J. Neurochem.* 73:961–971. http://dx.doi.org/10.1046/j.1471-4159.1999.0730961.x

Sidi, S., T. Sanda, R.D. Kennedy, A.T. Hagen, C.A. Jette, R. Hoffmans, J. Pascual, S. Imamura, S. Kishi, J.F. Amatruda, et al. 2008. Chk1 suppresses a caspase-2 apoptotic response to DNA damage that bypasses p53, Bcl-2, and caspase-3. *Cell*. 133:864–877. http://dx.doi.org/10.1016/j.cell.2008.03.037

Simon, D.J., R.M. Weimer, T. McLaughlin, D. Kallop, K. Stanger, J. Yang, D.D. O'Leary, R.N. Hannoush, and M. Tessier-Lavigne. 2012. A caspase cascade regulating developmental axon degeneration. *J. Neurosci.* 32:17540–17553. http://dx.doi.org/10.1523/JNEUROSCI.3012-12.2012

Smear, M.C., H.W. Tao, W. Staub, M.B. Orger, N.J. Gosse, Y. Liu, K. Takahashi, M.M. Poo, and H. Baier. 2007. Vesicular glutamate transport at a central synapse limits the acuity of visual perception in zebrafish. *Neuron*. 53:65–77. http://dx.doi.org/10.1016/j.neuron.2006.12.013

Steiner, M.R., F.W. Holtsberg, J.N. Keller, M.P. Mattson, and S.M. Steiner. 2000. Lysophosphatidic acid induction of neuronal apoptosis and necrosis. *Ann. NY Acad. Sci.* 905:132–141. http://dx.doi.org/10.1111/j.1749-6632.2000.tb06545.x

Steward, O., and E.M. Schuman. 2003. Compartmentalized synthesis and degradation of proteins in neurons. *Neuron*. 40:347–359. http://dx.doi.org/10.1016/S0896-6273(03)00635-4

Stuermer, C.A. 1988. Retinotopic organization of the developing retinotectal projection in the zebrafish embryo. *J. Neurosci.* 8:4513–4530.

Takemoto, K., T. Nagai, A. Miyawaki, and M. Miura. 2003. Spatio-temporal activation of caspase revealed by indicator that is insensitive to environmental effects. *J. Cell Biol.* 160:235–243. http://dx.doi.org/10.1083/jcb.200207111

Takemoto, K., E. Kuranaga, A. Tonoki, T. Nagai, A. Miyawaki, and M. Miura. 2007. Local initiation of caspase activation in *Drosophila* salivary gland programmed cell death in vivo. *Proc. Natl. Acad. Sci. USA*. 104:13367–13372. http://dx.doi.org/10.1073/pnas.0702733104

Timmer, J.C., and G.S. Salvesen. 2007. Caspase substrates. *Cell Death Differ.* 14:66–72. http://dx.doi.org/10.1038/sj.cdd.4402059

Ulukaya, E., C. Acilan, and Y. Yilmaz. 2011. Apoptosis: why and how does it occur in biology? *Cell Biochem. Funct.* 29:468–480. http://dx.doi.org/10.1002/cbf.1774

Waites, C.L., A.M. Craig, and C.C. Garner. 2005. Mechanisms of vertebrate synaptogenesis. *Annu. Rev. Neurosci.* 28:251–274. http://dx.doi.org/10.1146/annurev.neuro.27.070203.144336

Williams, D.W., S. Kondo, A. Krzyzanowska, Y. Hiromi, and J.W. Truman. 2006. Local caspase activity directs engulfment of dendrites during pruning. *Nat. Neurosci.* 9:1234–1236. http://dx.doi.org/10.1038/nn1774

Wishart, T.M., S.H. Parson, and T.H. Gillingwater. 2006. Synaptic vulnerability in neurodegenerative disease. *J. Neuropathol. Exp. Neurol.* 65:733–739. http://dx.doi.org/10.1097/01.jnen.0000228202.35163.c4

Wong, M. 2008. Stabilizing dendritic structure as a novel therapeutic approach for epilepsy. *Expert Rev. Neurother.* 8:907–915. http://dx.doi.org/10.1586/14737175.8.6.907

Wyatt, C., A. Ebert, M.M. Reimer, K. Rasband, M. Hardy, C.B. Chien, T. Becker, and C.G. Becker. 2010. Analysis of the astray/robo2 zebrafish mutant reveals that degenerating tracts do not provide strong guidance cues for regenerating optic axons. *J. Neurosci.* 30:13838–13849. http://dx.doi.org/10.1523/JNEUROSCI.3846-10.2010

Xiao, T., W. Staub, E. Robles, N.J. Gosse, G.J. Cole, and H. Baier. 2011. Assembly of lamina-specific neuronal connections by slit bound to type IV collagen. *Cell*. 146:164–176. http://dx.doi.org/10.1016/j.cell.2011.06.016

Yabu, T., S. Kishi, T. Okazaki, and M. Yamashita. 2001. Characterization of zebrafish caspase-3 and induction of apoptosis through ceramide generation in fish fathead minnow tailbud cells and zebrafish embryo. *Biochem. J.* 360:39–47. http://dx.doi.org/10.1042/0264-6021:3600039

Yamashita, M., N. Mizusawa, M. Hojo, and T. Yabu. 2008. Extensive apoptosis and abnormal morphogenesis in pro-caspase-3 transgenic zebrafish during development. *J. Exp. Biol.* 211:1874–1881. http://dx.doi.org/10.1242/jeb.012690

Zinsmaier, K.E., M. Babic, and G.J. Russo. 2009. Mitochondrial transport dynamics in axons and dendrites. *Results Probl. Cell Differ.* 48:107–139.